FACULTY OF SCIENCE AND TECHNOLOGY

MASTER THESIS

Study programme / specialisation:
Marine and Offshore Technology

The spring semester, 2022

Open / ~~Confidential~~

Author:
Terje Andreas Jevnaker

Course coordinator:
Professor Yihan Xing

Supervisors:
Professor Yihan Xing, University of Stavanger
Yucong Ma, University of Stavanger

Thesis title:
Station Keeping of a Subsea Shuttle Tanker System Under Extreme Current During Offloading

Credits (ECTS):
30

Keywords:
Submarine
ACER method
Extreme response
LQR
Station keeping
Extra-large AUV

Pages: 67

+ appendix: 23

Stavanger, 15/06/2022
date/year

Station Keeping of a Subsea Shuttle Tanker System Under Extreme Current During Offloading

June 15th, 2022

Submitted by:

Terje Andreas Jevnaker (257880)

Supervisors:

Professor Yihan Xing

Yucong Ma

ACKNOWLEDGEMENTS

The writing of *Station Keeping of a Subsea Shuttle Tanker System Under Extreme Current During Offloading* brings my two-year Master of Science program in Marine and Offshore Technology at the University of Stavanger to an end.

I want to express my deepest gratitude to Professor Yihan Xing for his teaching methods and ways of communicating his knowledge. His support and fruitful discussions will not be forgotten.

I would also like to extend my most sincere thanks to Yucong Ma for his guidance, knowledge sharing, and unanimous support throughout the writing of the thesis. Help was always available when needed, which has been highly appreciated.

Special thanks go out to the University of Stavanger, its staff, teachers, professors, and fellow students. All assistance and motivation have been highly valued.

Terje Andreas Jevnaker

University of Stavanger

Stavanger June 15th, 2022

ABSTRACT

A subsea shuttle tanker has been proposed as a multipurpose, versatile transport and storage system. This paper presents the station keeping challenge of the subsea shuttle tanker design during underwater loading and offloading at a subsea well under an extreme current environment. Understanding the behaviour of the proposed subsea shuttle tanker during offloading in extreme currents is vital for both the design of the subsea shuttle tanker itself but also the required actuator effort needed to uphold the demanded station keeping abilities. During the offloading process, the hoovering subsea shuttle tanker would current-vane in a water depth of approximately 70 metres. Recent studies have shown that the drag force exerted on the subsea shuttle tanker body is up to 80 times larger for side-ways current compared to the head-on current. With current-waning capabilities, the generated lift forces are low, and thus the subsea shuttle tanker will use less effort to maintain its desired position and water depth. The paper further investigates the movement of the subsea shuttle tanker during offloading with extreme current speeds, i.e., above 1.6 m/s, in the surge, heave, and pitch motions, respectively. The planar model is built up using a Luenberger observer, where the vessel motions are measured and fed into a linear quadratic regulator (LQR) for calculations of the control input. The LQR control's primary focus is to hold and achieve the target for the subsea shuttle tanker during the offloading process, i.e., minimize the horizontal and vertical motion. Finally, a state-of-the-art probabilistic method is used to predict the maximum potential displacement during offloading, i.e., the Average Exceedance Rate Method.

TABLE OF CONTENTS

LIST OF FIGURES

LIST OF TABLES

LIST OF ABBREVIATIONS

ABET	Accreditation Board for Engineering and Technology
ACER	Average conditional exceedance rate
AI	Artificial intelligence
API	American Petroleum Institute
ASME	The American Society of Mechanical Engineers
AUV	Autonomous underwater vehicle
bbl	Barrels
CCS	Carbon capture and storage
CCUS	Carbon capture, utilisation, and storage
CI	Confidence interval
COB	Centre of buoyancy
COG	Centre of gravity
DNV	Det Norske Veritas
DNV-GL	Det Norske Veritas-Germanischer Lloyd
DWT	Deadweight tonnage
ECEF	Earth Centred Earth Fixed
ECPD	The American Engineers' Council for Professional Development
EIA	Energy Information Administration
EOR	Enhanced oil recovery
EPA	The United States Environmental Protection Agency
GNC	Guidance, navigation, and control
IIoT	Industrial internet of things
IMO	International Maritime Organization
LQR	Linear quadratic regulator
MASS	Maritime autonomous surface ship
NFA	Norwegian Society of Automatic Control
NOAA	National Oceanic and Atmospheric Administration
NSIDC	National Snow and Ice Data Center
OPEC	The Organization of the Petroleum Exporting Countries
PID	Proportional-integral-derivative
QPC	Quasi-propulsive coefficient

ROV	Remotely operated vehicle
SST	Subsea shuttle tanker
UNECA	United Nations Economic Commission for Africa
UNFCCC	United Nations Framework Convention on Climate Change
WGS	World Geodetic System
WTI	West Texas Intermediate

1 INTRODUCTION

Marine and offshore engineering is a complex and multidisciplinary field. From ancient times to this very day, humankind has always faced practical problems which required practical solutions. Transportation of water, fabrication of weapons and aids for hunting, building houses and habitats for living and shelter, and production of electricity for heating and light are a few of the challenges that have been overcome due to clever minds and the willingness to explore. Other engineering achievements such as the pyramids in Egypt, Teotihuacan in Mexico and the Great Wall of China are extraordinary accomplishments, especially when considering the period when they were built.

Humans have always adapted to the environment for survival, which is a crucial factor in how far we have come today. Nomads, such as hunter-gatherers, moved cyclically between geographic places following seasonally available food, plants, water, and other necessities for living and endurance. The discovery of fire during what we believe is the early Stone Age is seen as one of the epochal achievements of its time (Harms, Baetx, & Volti, 2005) and was a giant leap toward a more safe and predictable life. Controlling and maintaining fire aided human evolution by keeping them warm, being a source of light, preparing and managing food and warding off animals and predators during nighttime. Modern civilization with advanced agricultural practices and state-of-the-art technological equipment has substituted the nomadic lifestyle with farming and contemporary living, i.e., the focus has shifted from a question of survival to how we can live as comfortable as possible.

The word *engineer* is derived from the two Latin words *ingeniare* and *ingenium*, which spells out: to contrive, device, and cleverness. A more defined description of the engineering role was provided by ECPD, The American Engineers´ Council for Professional Development (today known as ABET, Accreditation Board for Engineering and Technology):

"*The creative application of scientific principles to design or develop structures, machines, apparatus, or manufacturing processes, or works utilizing them singly or in combination; or to construct or operate the same with full cognizance of their design; or to forecast their behaviour under specific operating conditions; all as respects an intended function, economics of operation and safety to life and property*".

Within modern engineering disciplines, multiple branches are established, where each branch is specialized within defined technologies and concepts. The continuous improvement of

technology, science and knowledge has given us greater possibilities than what humankind earlier believed impossible. We have put people on the Moon, obtained images from Mars and commercialised air travel. Our understanding of Earth and the Universe evolves every day, and we continue to explore its complexity.

Above 2/3 of the Earth's surface is covered with water. Even though many activities are carried out above and under the sea surface, deep-sea explorations are still considered in the early stages.
What is next for the marine and offshore industry? The business has been driven by the economic possibilities, the essential need for energy or merely out of human curiosity. In recent years profitability and labour-effective projects and processes have been the focal point as more focus has been put on cost management. In addition, the impact on the environmental footprint and safety throughout the business are vital factors when moving towards energy transition and *net zero*[1].

I hope and believe that the work completed in this thesis will contribute to the knowledge database and excite the readers, and arouse interest in marine and offshore technology, global warming, and carbon capture and storage (CCS).

1.1 Background

Oil and gas in the offshore environment have been evolving rapidly since 1947, when the first successful offshore well was drilled in the Gulf of Mexico (Bai & Bai, 2018). With population growth and technological development, the energy demand has been steadily expanding over the last seven decades. Figure 1.1 displays the increase in the consumption of oil, coal, natural gas, wind/solar/geothermal power, hydropower, nuclear power, and biomass from 1980 to predicted 2030.

[1] Achieving balance between the produced /emitted greenhouse gas emissions and emissions removed from the atmosphere.

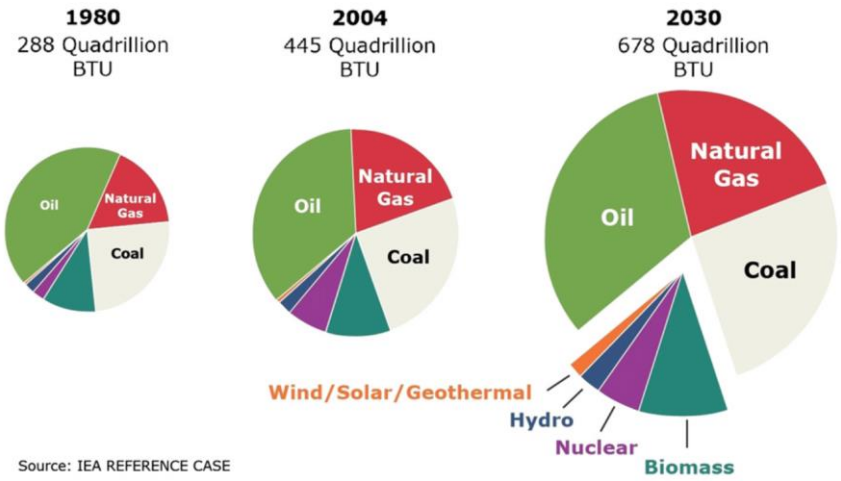

Figure 1.1. Increase in oil, coal, and natural gas consumption **(Bai & Bai, 2018)**.

Supply and demand, together with exploration and production costs, have always governed the price of oil and gas in the retail and consumer market. Over the years, it has shown, at times, to be highly volatile. In the long run, there are four parameters and trends that influence the price (Huntington, Al-Fattah, Huang, Gucwa, & Nouria, 2014): global economic growth, demand-side technological progress and efficiency gains, new alternative energy sources and the changing cost of production.

The spread (Macrotrends, 2022) of the West Texas Intermediate (WTI) crude oil price per barrel from 1946 to 2021 is presented in Figure 1.2 and has been adjusted according to the inflation rates.

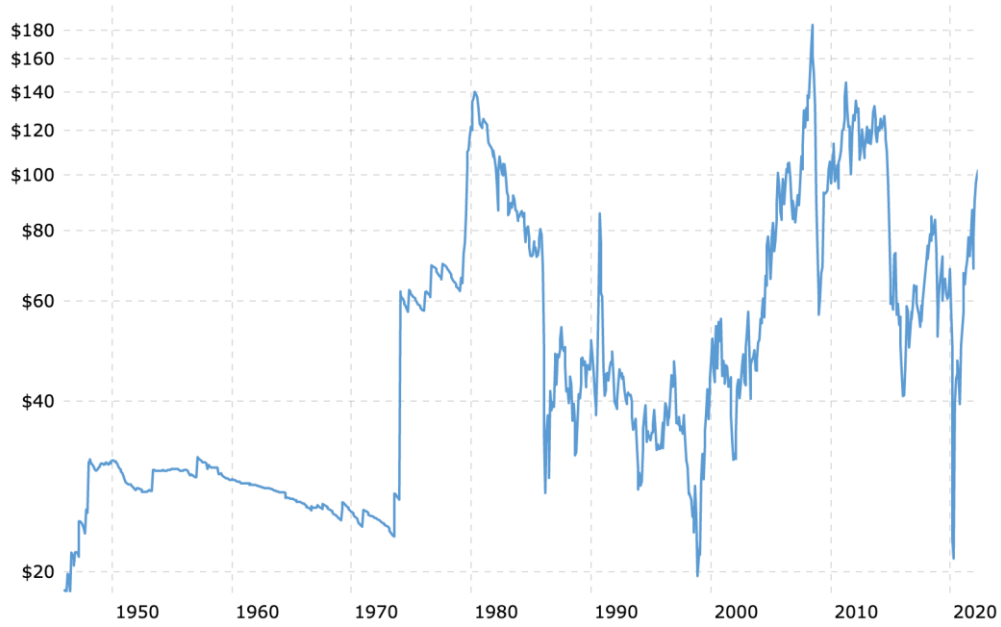

Figure 1.2. Crude oil price per barrel, WTI 1946-2021 **(Harms, Baetx, & Volti, 2005)**.

As the chart manifests, the price has changed significantly during specific periods. Until the early 1970s, the price was more or less stable before the price experienced a steep increase due to an oil embargo by Arab producers against the United States (Maugeri, 2006). In 1979 the price reached new heights due to the Iran-Iraq war. After this, the oil price gradually fell until we saw another spike in 1990 when the Gulf war started. An all-time-low came in 1998 at around 19 USD/bbl., mainly due to the economic recession in Asia and the Pacific region (Lichtblau, 1999). The highest value was reached in 2008 before the global financial collapse made the price plummet. After the outbreak of the Covid-19 pandemic, demand was reduced due to travel restrictions and near-future uncertainties, which made the price fall significantly. Recent geopolitical events and Russia's invasion of Ukraine have caused the oil price to rise, and by mid-April 2022, it was traded at above 100 USD/bbl.

In today's market, oil and gas are traded at different locations, with specific grades and qualities. As the quality of the produced oil and gas may vary depending on the geographic area it has been produced; the industry often divides the quality into six different classes (Platts, 2022): heavy/sweet, heavy/sour, medium/sweet, medium/sour, light/sweet and light/sour.

The six types of crude oil are used in different applications and have different properties. Heavy crude oils have a higher density compared to the lighter crude oils, and sweet crude oils have lower amounts of sulphur compared to the sour crude oils. Liquid petroleum with

API gravity of less than 20° is regarded as heavy (Speight, Fantacci, & Speight, 2011). Liquid petroleum with sulphur content above 0.5 % is considered sour. Sour crudes require more refining to remove unwanted impurities, which add to the total cost of the product. Environmental regulations often limit the allowable sulphur content in end products, including gasoline and diesel. The International Maritime Organization, IMO 2020 (IMO, 2020), which came into effect in January 2020, defines the limit of the allowable sulphur content in fuel oil used for ships in the maritime sector. Traditionally, ships have been using heavy fuel oil, but the new limits compel the shipping companies to move over to very low sulphur fuel oils. Based on the new boundaries, it was forecasted that an overall reduction of 77 % in sulphur oxide emissions from ships could be achieved. This is seen as a significant decrease and will have substantial positive effects on health and the environment, especially for coastal and port areas.

In the market of buying and selling crude oil, several benchmark brands have been introduced, acting as references, and defining the spot value of the product (Scheitrum, Carter, & Revoredo-Giha, 2018). The three most common and well-known benchmark crude oils (Speight, Fantacci, & Speight, 2011) are the *West Texas Intermediate* (WTI), *Brent Blend* and *Dubai Crude*. WTI is a light and sweet crude oil most commonly used in the U.S. The Brent Blend, or Brent Crude, is also a light (slightly heavier than WTI) and sweet crude oil and is the primary universal price benchmark for the Atlantic crude oils. Dubai Crude is medium/heavy and sour crude oil produced in Dubai and is mainly used for pricing the export of oil to Asia. Other frequently used benchmarks are the *OPEC Reference Basket* (ORB), *Minas*, and *Bonny light*, which originate from OPEC countries, the island of Sumatra and Nigeria, respectively.

Motivation for exploration and investments in potential petroleum projects may vary based on the applicable petroleum fiscal agreements. Economic analyses will be conducted as a means to make decisions on whether to move forward or not with a proposed field development. Parameters such as cash flow analysis, inflation, deflation, net present value, break-even price, and risk and sensitivity analyses will be assessed and calculated. The produced oil and gas belong to the oil and gas producing country, and government revenues are created either by royalty (i.e., taking a share of the produced crude oil through contract or direct participation through a licencing system) or by putting a tax on the company profits (Odland, 2020). The taxation scheme will vary and depend on the agreed terms between all

parties. It is essential to make potential investments attractive, as the cost of exploration and development is often the most significant. Oil companies frequently create joint venture agreements, where several parties align forces in search, development, and production projects. The sheer size and nature of the required investments and the complex tasks involved in the search and production of oil and gas are best handled when they are shared. By doing this, companies can lower and spread the risk and share knowledge and capital within the joint venture.

Subsea pipelines and tanker ships have been utilised to transport oil and gas from offshore subsea fields to onshore facilities for refinement and delivery to the end consumer. The transportation of crude oil and gas products from production sites to refineries and end consumers has always been a challenge since early explorations and onshore drilling activities back in the 1860s. Moving the product in a safe and economically viable way over long distances was difficult in the early days, and several solutions have been brought into service over the years. From 1859 when the Drake oil well (ASME, 2022), considered the first practical oil recovery system, was drilled, the crude oil was transported in carts by wooden barrels, where converted whiskey, beer or fish casks were often used. Therefore, we often see production rates and oil prices in terms of bbl., or barrels of oil.
As the energy demand increased with production rates, barrels were soon exchanged with wooden and steel pipelines. The escalating oil production also sped up the development of the transportation infrastructure, and thus trucks could be used for delivery where pipelines were difficult or impractical to build. Moving crude oil overseas was done as early as 1861 (The Maritime Industry Knowledge Center, 2022) when the brig Elisabeth Watts carried 224 tonnes of petroleum substance. For comparison, today's ultra-large-crude-tankers have a capacity of 320-550,000 DWT, deadweight tonnage[2] (Hamilton, 2014).

Most of the readily available and recoverable oil and gas resources have already been produced in the modern age. The oil and gas industry has thus moved further offshore, and production and transport of oil equivalents are being completed at water depths > 2000 m, generally categorised as ultra-deepwater. Engineering and applied science have come a long way, and newly developed fields utilise advanced and maturing technologies such as subsea processing (i.e., separation, boosting and compression of fluids) and continuously improving

[2] Maximum weight (i.e., fuel, cargo, fresh water, ballast water, passengers, crew, and supplies) a ship can carry.

enhanced oil recovery methods. These methods, among others, do provide the offshore operators with the possibility of life extension for many of the original field developments. An example of this is Equinor on the Norwegian continental shelf, which between 2016 and 2019, got a lifetime extension for 8 installations, ranging from 12 to 20 additional years (Equinor, 2019).

Global CO_2 emissions have increased in conjunction with developing energy expenditure, and from 1970 to 2014, they rose by as much as 90 % (EPA, 2022). According to a press release (IEA, 2022) in April 2020, "*IEA report sees global energy-related CO_2 emissions rising by 1.5 billion tonnes in 2021, driven by a strong rebound in demand for coal in electricity generation*". After experiencing a decline in CO_2 emissions since the COVID-19 pandemic, this will be the second-largest increase in history and the most significant since 2010.

The Paris Agreement (UNFCCC, 2022), adopted by 192 states and the EU, a legally binding international treaty, focuses on the international climate and climate change. By setting the overall target of limiting global warming to 2 ° C compared to pre-industrial levels, the aim is to slow and reduce the effects of global warming. There has been a rapid rise in the surface temperature of the planet in recent years (NOAA, 2022), and the earth's temperature has risen 0.18 ° C per decade since 1981. This is a significant increase compared to earlier levels, and the 10 warmest years recorded to date have all taken place from 2005 onwards. The temperature rise generates more extreme and unpredictable weather and climate effects. It contributes to higher sea levels, habitat disruptions, severe droughts, and heatwaves, to mention a few of the concerning issues (Frank, et al., 2015).

The earth's early history shows that climate changes were fundamental parts of the evolution of the continents (Sorensen B. , 2011). The evolving and changing climate also played a significant role in forming the atmosphere and the oceans. The extensive destruction of natural vegetation is one of the first consequential anthropogenic influences on the climate. The introduction of farmable and grazing land has affected the net energy flux of the earth's surface, i.e., the balance between the incoming and outgoing energy in the atmosphere.

It is essential to understand that climate change is an *ongoing* process, and the impact can be observed and experienced every day. The climate influences the ecosystem in many ways. Rising seawater levels can cause more saltwater mixing in freshwater networks and may

affect the species at these locations. In the Arctic region (NSIDC(1), 2022), sea ice measurements have been carried out for several years, and Figure 1.3 clearly shows the downward trend in the Arctic Sea ice extent. Effects of this continued loss of the Arctic Sea ice (NSIDC(2), 2022) include erosion of the Arctic coastline, interruption of the global weather pattern, and further Arctic and global warming. All these changes and interruptions will influence the entire fauna and flora in the Arctic region.

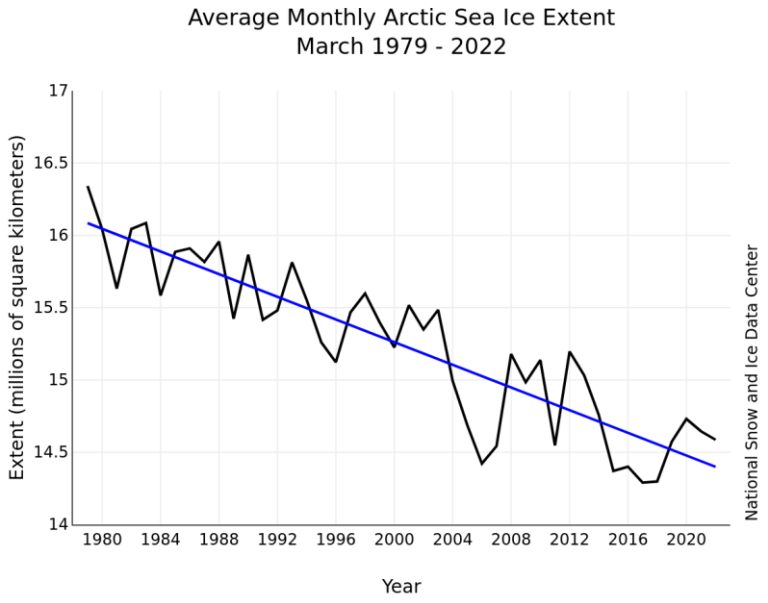

Figure 1.3. Average monthly Arctic Sea ice extent March 1979-2022 **(NSIDC(1), 2022)**.

Annual CO_2 emissions (Our World in Data, 2022) from the burning of fossil fuels, including oil, gas, coal, flaring, cement production, and land-use change, are presented in Figure 1.4, and the graph clearly shows a steady increase over the last 70 years.

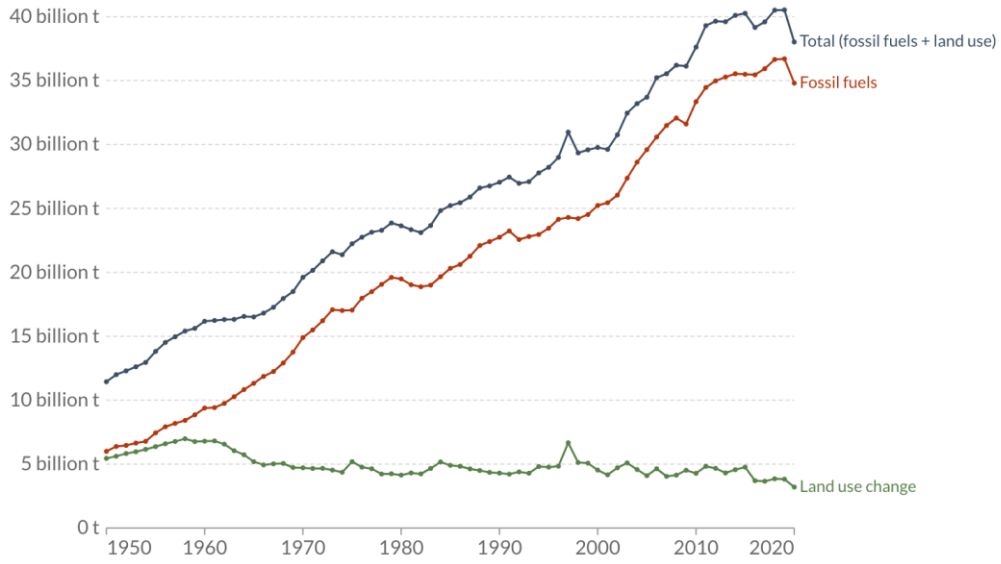

Figure 1.4. Annual CO_2 emissions 1950-2020 **(Our World in Data, 2022)**.

To meet the target depicted in the Paris Agreement, the reduction of the industrial CO_2 footprint will be of high importance. The release of greenhouse gases emitted from burning oil and gas, or coal, either for use in the industry, creating heat and electricity, or creating mechanical energy through combustion engines, can be mitigated by CCS. The CCS aims to capture and store the CO_2 before it's released into the atmosphere. This will play a vital role moving forward, as fossil fuels still provide most of the electricity, and energy plants are often fuelled by coal and gas (IEA, 2020).

The future of CCS is a frequently discussed topic, both in media and the academic environment. Equinor's annual energy perspective from 2021 (Equinor, 2021) predicts an uncertain future for energy transition and sustainability. Access to energy is a certainty for most developed countries, while less developed regions such as Asia and Africa see an increase in demand as they are continuously maturing. Infrastructure is improved, living standards rise, and thus the energy requirements will follow. Renewable energy sources in developing countries often have great potential. Still, economic development depends not only on energy but also on the stability and quality of the energy itself, i.e., governments rely on investments and commitments from energy companies. Central Africa, a developing region, has shown significant economic growth rates over the last couple of decades (UNECA, 2021). However, the energy sector in the area is still heavily relying on the production and export of raw materials, such as crude oil. As the global trend moves towards a *net zero* target and decarbonization, crude oil prices and similar commodities will be

vulnerable to significant and sudden changes. Countries like China and India are approaching renewable energy development as part of the industrialisation to be better prepared for future energy needs while also considering the environment. The Renewable Energy Country Attractiveness Index (RECAI) (EY Global Power & Utilities, 2021) ranked China and India second and third, respectively, in October 2021, confirming their attractiveness in the renewable energy deployment and investment opportunities.

bp *Energy Outlook* evaluates the current and future energy trends and needs. For the 2022 edition (bp, 2022), the focus is on three different scenarios: *accelerated*, *net zero* and *new momentum*. These scenarios are used to explore and analyse the energy transition towards 2050. By examining the possible outcomes, potentially relevant information on which measures needed to be put into place to reach the overall *net zero target* may be identified. There are solid trends in addressing the climate change issue worldwide. Global ambitions within renewable energy sources are increasing as the attention is shifted toward low-carbon energy systems such as new wind and solar energy projects, electric vehicle sales, hydrogen technology, and CCS/CCUS projects. Through governmental and political enforcement, measures such as tighter carbon emission policies and funding of research and development programs in clean technologies will stimulate and highlight the importance and recognition for policymakers and the public eye.

In Figure 1.5 all commercial CCS facilities as of 2021 (Global CCS Institute (1), 2021) are presented, including already operating establishments and projects under construction or in advanced development. As can be seen, there are already several running fields either used for enhanced oil recovery or as dedicated geological storage sites. By looking at the trend, the CCS facilities are also moving more into areas like power generation, cement production, iron and steel production, and waste to energy. The Prairie State Generation Station Carbon Capture project (Global CCS Institute (2), 2021), planned to be operational in the mid-2020s, will alone seek to facilitate a 50+ million tonne commercial storage hub in the US.

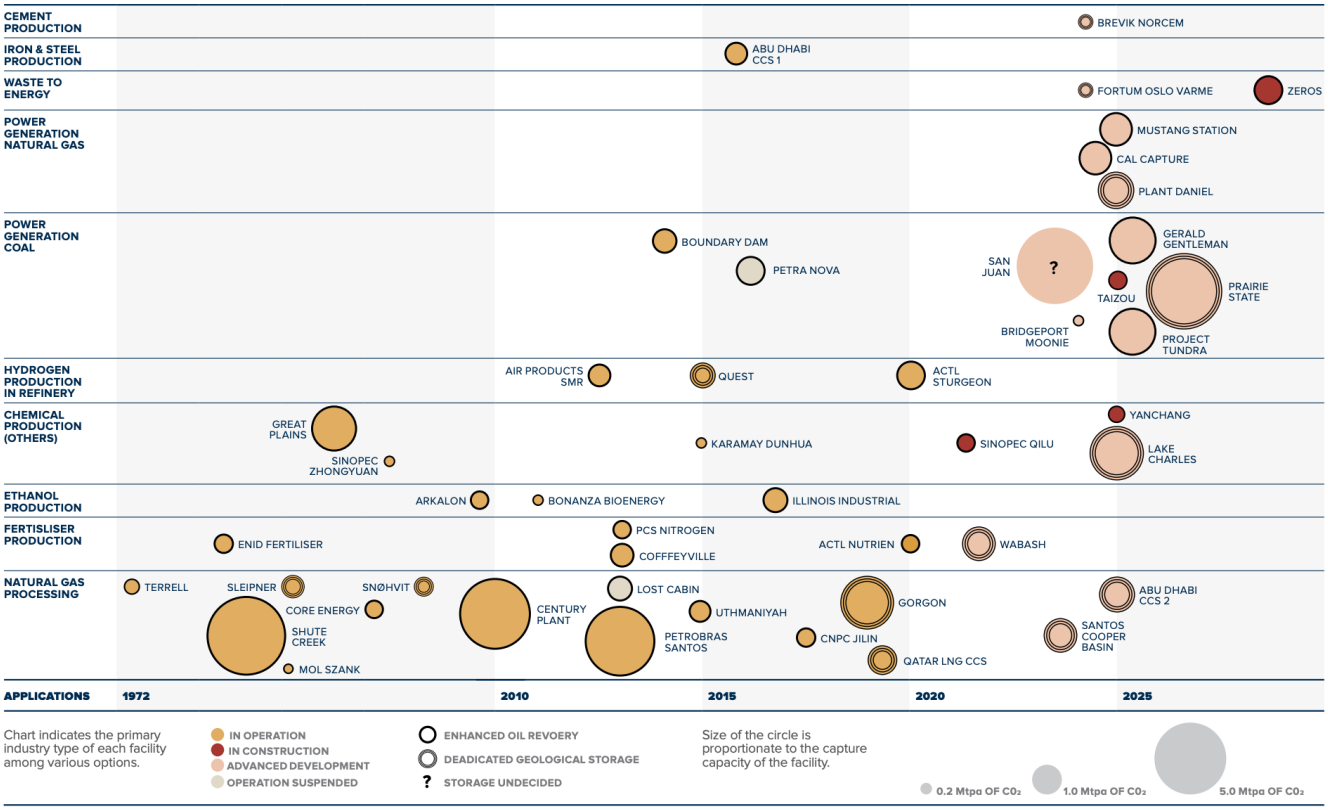

Figure 1.5. Commercial-CCS projects as of May 2021 **(Global CCS Institute (1), 2021)**.

1.2 SST Design

The SST is proposed (Ma, Xing, Ong, & Hemmingsen, 2021) as an alternative for the transportation of liquid carbon dioxide and the authors completed a 34,000-tonne baseline design. The SST concept illustrated in Figure 1.6 was first introduced in two research disclosures by Equinor (Ellingsen, et al., 2020) (Equinor ASA, 2019), where multiple freight submersible concepts were proposed, such as train-like AUV, subsea glider, and SST. (Xing, Ong, Hemmingsen, Ellingsen, & Reinås, 2021a) focused on the SST concept and entailed the most critical design considerations of using civilian submersibles to transport liquid carbon dioxide. The design offers the possibility of utilizing smaller and remote subsea wells and reservoirs for permanent CO_2 storage. As many of the current CCS projects rely on pipelines for pumping CO_2 into the reservoirs, this is not economically feasible for smaller and more marginal subsea field developments. Pipeline design, production and installation costs are high, and it is preferred to take advantage of existing infrastructure.

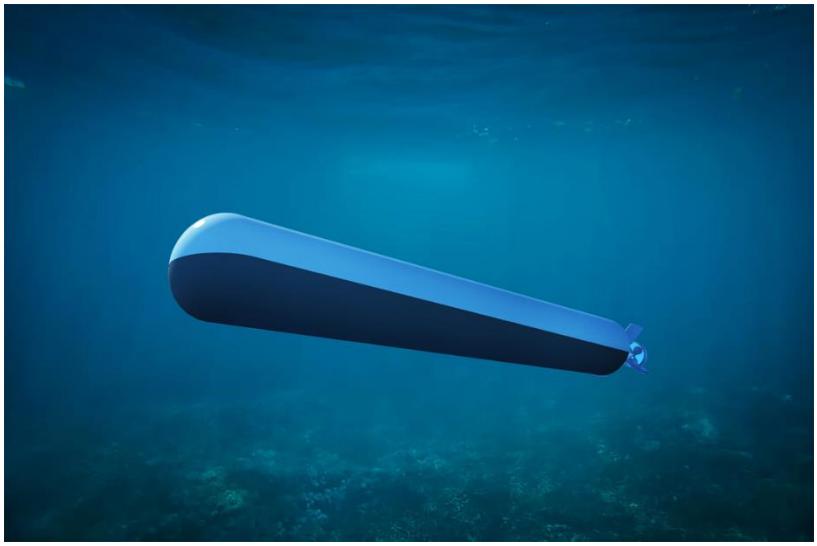

Figure 1.6. SST graphic.

With an increasing global demand for energy, the CCS solutions and storage site capacity must also follow, focusing on *net zero* and the Paris Agreement target.

In theory, the SST could also store, or transport other liquids used in the marine industry, e.g., oil, gas, MEG, or similar chemicals used for offshore operations (Equinor ASA, 2019). For remote fields where subsea pipelines are not viable due to cost or complexity, the SST can provide the desired characteristics, both concerning transportation volume, capacity, and operational limits. Compared to offshore tankers, which are vastly weather dependent during transportation, loading and unloading, the SST could operate in a harsher environment as its normal working depth is 70 m.

In addition, the SST can help to mitigate climate change and advance the industry towards net zero as it is electrically propelled and therefore has zero carbon footprint during transportation. This contributes to the maritime industry's sustainability, which accounts for roughly 3.3% of the CO_2 emission resulting from fossil fuels (Papanikolaou, 2014). A technical-economic study found that the SST can become the enabler to the utilisation of subsea fields with an annual storage capacity below 2.5 million 60 tonnes per annual for carbon storage projects (Xing, Santoso, & Ma., 2021b).

The SST general arrangement is presented in Figure 1.7. A shows the cross-section at midship, including the main cargo tank, auxiliary cargo tank and external hull. B shows the SST forward bulkhead with a free flooding bow apartment, including a compensation tank and trim tank. C shows the SST aft bulkhead, with a free flooding aft apartment, including a

second compensation tank and trim tank. D shows the buoyancy tanks and their direct connection through the bulkheads.

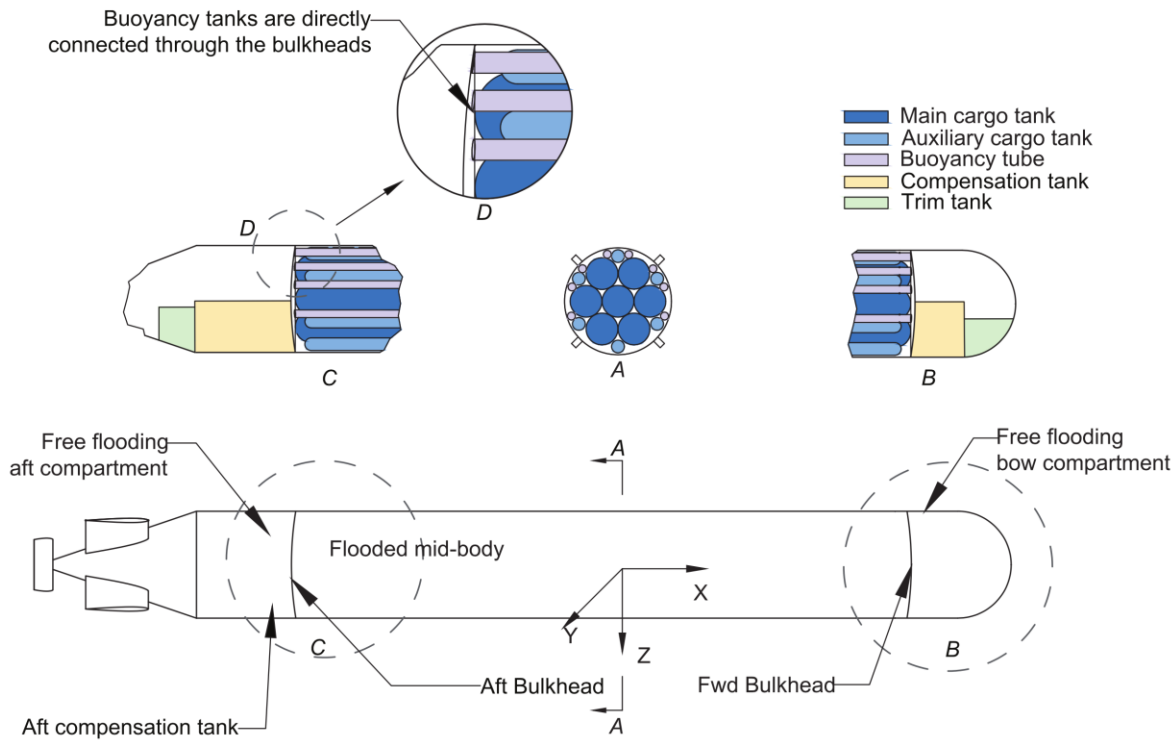

Figure 1.7. SST general arrangement **(Ma, Xing, Ong, & Hemmingsen, 2021)**.

The free flooding compartment at the bow contains vital communication and monitoring equipment such as sonar, radio, sensors, and a control station. It also houses the forward trim and compensation tanks and pumps for CO_2 offloading. In the aft, the free flooding compartment consists of propulsion and mechanical apparatus such as gearbox and motor, battery, and rudder controls and the aft trim and compensation tanks. The flooded mid-body, the most extensive section of the SST, contains the general piping, cargo, and buoyancy tanks.

According to the Norwegian CCS Research Centre (SINTEF/The Norwegian CCS, 2020) and IEA (IEA, 2019), 14 % of the total global emissions reduction must come from carbon, capture, and storage technologies within 2060. CSS is already proven technology, and on the Norwegian continental shelf, CO_2 has been stored at the Sleipner field since 1996, approximately 1 million tonnes per year (SINTEF/The Norwegian CCS, 2020). Enhanced oil recovery methods (EOR) have also included the injection of CO_2 into maturing subsea fields, which have been done for the last 4 decades (Global CCS Institute (3), 2021). This has helped rejuvenate oil production for ageing subsea fields, where production rates have declined due

to depletion of the original reservoir pressure. By doing this, more crude oil has been produced, and CO_2 has been permanently stored in the subsea wells.
The proposed subsea shuttle design with a total length of 164 m, a beam of 17 m and a full storage capacity of 16,362 m^3 is shown to fulfil the Norwegian annual storage demands of the ongoing CCS projects (as of 2021).
The methodology of the proposed design is based on the mission requirements where cargo capacity, necessary depth range and relevant environmental data are considered. The design range is 400 km, which originates from the distance of the existing and planned CSS storage sites on the Norwegian continental shelf (two CCS storage sites are already active, Sleipner/Utgard and Snøhvit).

The Northern Lights Project (Northern Lights CCS, 2022) is a collaboration project between Equinor, Shell and Total, where the aim is to be the first open-source CO_2 transport and storage infrastructure.
The project is a part of Longship and is responsible for the transport and storage assets of the full-scale CCS program launched by the Norwegian Government (Fortum, 2022). Longship's objective is to capture CO_2, transport it to designated terminals, and utilise already existing subsea pipelines for pumping liquified CO_2 to deep underground reservoirs.

As mentioned previously in the thesis, a nominal diving depth of 70 m is based on the minimum recoverable lost-cause situation. This operating depth also provides suitable conditions for the SST as it moves underneath the wave-interaction zone, i.e., it experiences fewer hydrodynamic loads, which is beneficial for the power economy and advantageous for the design of the manoeuvring control system. To avoid collisions with floating ships and facilities, the safety depth is set to 40 m. SST test diving depth is defined as 105 m and collapse depth as 190 m. These values are in accordance with DNVGL-RU-NAVAL-Pt4Ch1 (DNV-GL, 2018). Test depth and collapse depth are based on 1.5 and 2.7 times the nominal diving depth, respectively.

The physical design of the SST is based on a double hull torpedo design with an active pressure compensating system. Such a torpedo-hull design offers a good balance between cargo volume and minimum drag resistance. This allows for a more economical and conservative design as the double hull with flooded mid-body will account for the varying external pressure loads. Achieving the desired structural integrity requires a high focus on the cost and safety aspect in the early design, as any redesign in a later stage may prove to be of a

high cost. If similar SSTs are to be designed in other regions of the world, there may be a big difference in metocean conditions as well as cargo capacity and energy requirements.
For the SST, it is essential to have the lowest possible power consumption without compromising the desired functionalities. Lesser energy the SST uses, the more operational up-time can be achieved, thus maximising the range. An optimal control approach, where the feedback gain is obtained for finding the desired actuator effort versus SST movement during offloading, is presented in chapter 3.

1.3 Autonomy and Dynamics

Autonomy is defined (NFA, 2012) as "*the ability of a system to achieve operational goals in complex domains by making decisions and executing actions on behalf of or in cooperation with humans"*. Going autonomous will offer advantages and challenges for the SST. The major challenges with autonomy compared to other subsea applications (i.e., ROV etc.) are often the navigation and communication between the vessel and control hub. Mission requirements and planning must be done upfront but means of communication are needed for the operators to verify that the mission is progressing as planned.

When developing autonomous systems in the maritime environment, the motivation arises from potential reduced operational costs and accountability. It is discussed by Karvonen and Martio (Karvonen & Martio, 2018) how human factors still play a vital role in the autonomy design of maritime autonomous surface ships (MASS). Essential aspects of a successful autonomy system are automation trust, automation capability and the opportunity for the operator to obtain a satisfactory report or status of the vessel. Having no operators on board will increase the need for knowing, e.g., the position and orientation of the vessel, and it will also influence the possibilities of manoeuvring any tight areas with constructions or other subsea or surface structures. Another drawback of not having humans on board is that any required in-field maintenance for the SST would be laborious and demanding.

Trust in automation can be underestimated when one thinks about designing and implementing autonomous systems. Several papers and studies have been written on the subject. John D. Kee and Katarina A. See (Lee & See, 2003) sum it up nicely: "*Trust influences reliance on automation; however, it does not determine reliance*". By gathering selected data, decisions are made, and processes are controlled. Even though one can argue that this will be highly beneficial regarding risk and safety from a holistic point of view, there is no rule without exception. History has shown that accidents *happen* either when automation is trusted entirely or when it is misused. As with all processes and activities, knowledge and lessons can always be taught when they are successful and when they fail.

Motions and degrees of freedom will be the same for subsea vehicles as for surface ships (Journée & Massie, 2001), presented in Figure 1.8. Translational motions (i.e., surge, sway, and heave) are in the x-, y- and z-direction and rotational movements (i.e., roll, pitch, and yaw) are about the x-, y-, and z-axis, respectively.

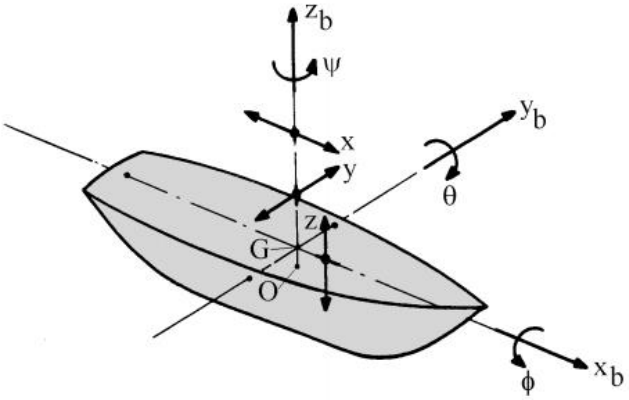

Figure 1.8. Definition of motions and six degrees of freedom **(Journée & Massie, 2001)**.

The dynamics of an autonomous underwater vehicle (AUV) are inherently nonlinear and time-variant (Ribeiro Mendes, Bentes, Rebelo, & Bousson, 2017), similar to a flying object. The forces experienced by the SST during transportation include buoyancy, thrust, weight, drag and lift. They also introduce the translational movement and rotational moments acting on the SST.

Newton's second law (Eq. (1)) states that the force F acting on a body is equal to the mass m of the body multiplied by the acceleration a.

$F = m \cdot a$	Eq. (1)

The equations of motion of the SST are presented in 2.2. These are based on the governing equations of motion for underwater vehicles in ocean current (Eq. (2)), and they are usually written (Li, 2016) as follows:

$\begin{cases} \dot{\eta} = F(\eta, \nu) \\ \dot{\nu} = G(\eta, \nu, t) \end{cases}$	Eq. (2)

The 6 degrees of freedom motion will derive a 12-dimensional nonlinear dynamical system where η denotes the position and ν denotes the velocity.

Levels of autonomy will depend on the system and its applications. Larger systems may include sub-systems that run autonomous, while other smaller applications like standalone robotics may be fully independent in performing their designated activities or tasks. Even though different definitions of autonomy levels have been described and used, Table 1.1 presents the overview defined by the US Navy Office of Naval Research (also introduced in (NFA, 2012)). It clearly states the different autonomy levels, and the description leaves little ambiguities about the additional requirements, which would be beneficial in any potential project and design process.

Table 1.1. Levels of autonomy **(NFA, 2012)** and US Navy Office of Naval Research.

Level	Name	Description
1	Human operated	All activity within the system is the direct result of human-initiated control inputs. The system has no autonomous control of its environment, although it may have information-only responses to sensed data.
2	Human assisted	The system can perform activity in parallel with human input, acting to augment the ability of the human to perform the desired activity, but has no ability to act without accompanying human input. An example is automobile automatic transmission and anti-skid brakes.
3	Human delegated	The system can perform limited control activity on a delegated basis. This level encompasses automatic flight controls, engine controls, and other low-level automation that must be activated or deactivated by a human input and act in mutual exclusion with human operation.
4	Human supervised	The system can perform a wide variety of activities given top-level permissions or direction by a human. The system provides sufficient insight into its internal operations and behaviours that it can be understood by its human supervisor and appropriately redirected. The system does not have the capability to self-initiate behaviours that are not within the scope of its current directed task.
5	Mixed initiative	Both the human and the system can initiate behaviours based on sensed data. The system can coordinate its behaviour with the human behaviours both explicitly and implicitly. The human can understand behaviours of the system in the same way that he understands his own behaviours. A variety of means are provided to regulate the authority of the system w.r.t. human operations.
6	Fully autonomous	The system requires no human intervention to perform any of its designated activities across all planned ranges of environmental conditions.

Autonomy and autonomous vehicles have been employed within military operations for over 75 years (Autonomous Vehicles in Support of Naval Operations, 2005). With the benefit of commissioned autonomous systems, we have seen an increasing focus on using autonomous equipment and services for the oil, gas, and shipping sectors. Reasons and motivation for this are often based on health, safety, and cost considerations and enabling more advanced robotic and monitoring equipment. A continuous improvement in technology also makes state-of-the-

art solutions more available and affordable. The development could include advances in artificial intelligence (AI) and machine learning in cooperation with the industrial internet of things[3] (IIoT) on the path toward a progressing and more sustainable future for the industry.

Through the years, large portions of the 'easier' available and recoverable resources have been produced, and continued exploration and production require further technological development and potentially autonomous systems.

1.4 Offloading, Station Keeping and Manoeuvrability

The SST is equipped with a single propeller, hydroplanes, and tunnel thrusters. Figure 1.9 and Figure 1.10 display the CO_2 offloading sequence and the environmental loads that the SST will be subjected to, such as hydrostatic pressure, wave loads in shallow water, and ocean current. The single propeller located at the aft contributes to SST movement during transport from the onshore facility to the offshore well and vice versa. The hydroplanes will assist in keeping the desired nominal diving depth of 70 m. When the CO_2 offloading location is close, forward movement will be reduced, and the generated lift forces will decrease. Maintaining the required depth control will be completed using the tunnel thrusters in collaboration with the ballast tank system. During this process, the SST will prepare for CO_2 discharge and hover in the region above the subsea well. Then, a remotely operated vehicle (ROV) deployed at the subsea well will launch and carry a flowline to mate with the SST. After the flowline is appropriately connected, the SST discharges CO_2 to the wellhead while it pumps in seawater to ensure neutral buoyancy. Finally, the ROV disconnects with the SST when this process is fulfilled. The entire offloading operation consumes 4 hours. Station keeping and hovering capabilities for subsea vehicles to maintain desired horizontal and vertical movement are constantly being investigated and researched. Numerous AUV designs and configurations have been proposed over the years for commercial, military, and scientific applications.

During CO_2 offloading, the station keeping ability plays a vital role in the safety and integrity of the SST, the flexible flowline, and connection points at the vessel and the subsea well. Suppose the station keeping system is not able to keep the SST within the acceptable range of

[3] Extension of internet of things and includes networked instruments and interconnected sensors for monitor and management systems.

the subsea well. In that case, the result may lead to broken connections due to snap loads between the flexible flowline and the SST or a sudden increase in the hydrostatic pressure due to heave motions. This scenario may lead to expensive repairs and maintenance requirements and reduced CO_2 transport and storage abilities due to potential damage to the subsea well connection and the SST.

Ocean current has the *most* considerable dynamic effects on the SST as it drives the SST to an off-site, away from its desired reference offloading position. Therefore, the SST uses its hovering system consisting of a propeller and two thrusters to cope with the ocean current load. Though the ballast system can account for the weight change during offloading, the thrusters will accommodate actuation at higher frequencies. A comprehensive understanding of the motion in extreme currents is vital to the SST design. A previous study shows that side-way current drag is 80 times greater than head-on current; the SST has to constantly head-on current while offloading (Ma, Xing, Da Silva, & Sui, 2022b). When the SST is facing ocean current, the surge off-site affects the required designed length of the flowline to avoid tautly and snap loads. The ocean current can also result in severe heave and pitch motions. This decides the maximum depth excursion of the SST, which determines the collapse pressure and is the dominating factor of the SST pressure hull design. The minimum depth excursion affects the safety depth (upper bound) of the SST during operation. Knowing this is essential for the SST to avoid collision with ships or other surface installations.

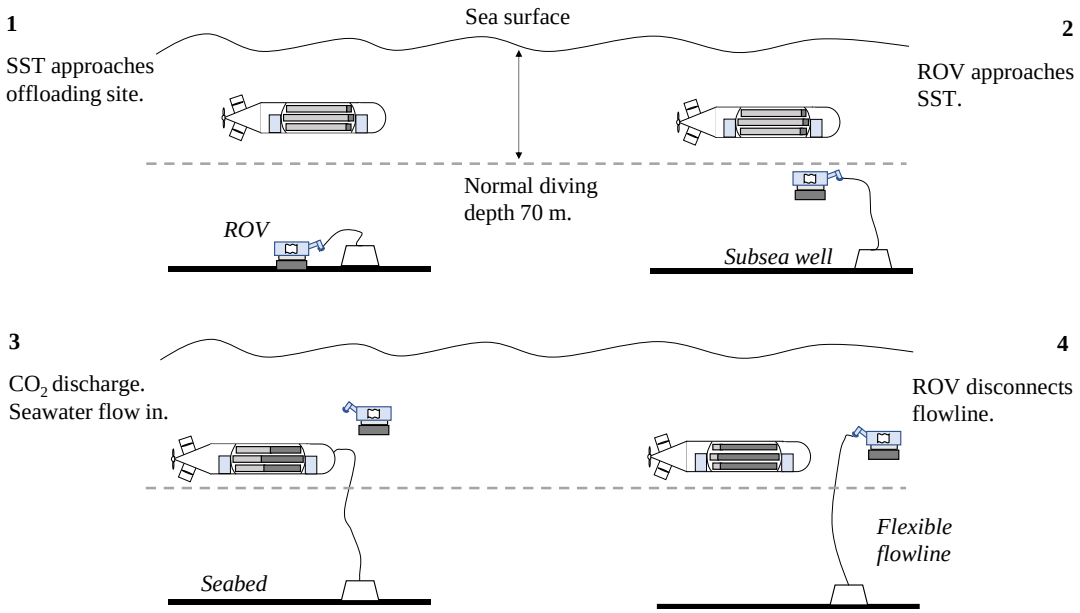

Figure 1.9. SST during unloading sequence.

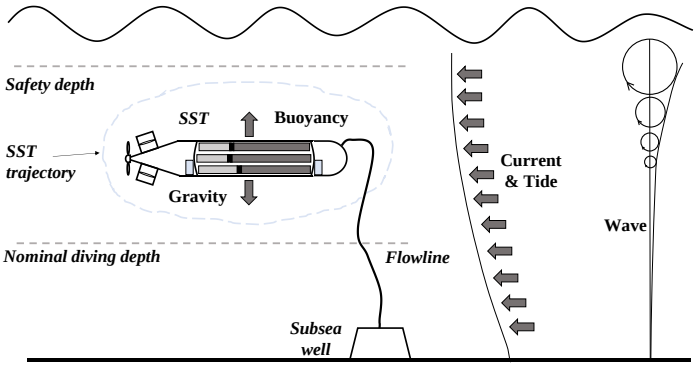

Figure 1.10. SST forces.

Therefore, the positional responses of the SST under extreme current are studied in this paper using the state-of-the-art averaged conditional exceedance rate (ACER) method. A 2D planar model together with a hovering control system is proposed and tuned by (Ma, Da Silva, Xing, & Sui, 2022a). The LQR control focuses on the non-linear models (rather than the linear model approach typically utilised by PID controllers) and offers robust stability with minimized energy expenditure. Later, this work is extended to investigate the SST depth excursion during aft thruster failure (Xing, Gaidai, Ma, Naess, & Wang, 2022), which found that response at the SST aft, where thruster failure happens, has a 1.3-2.6 times larger response than the SST bow. This work will focus on the integrated SST model but consider a 1.6 m/s extreme current speed and more considerable fluctuation. Also, disturbances during unloading will be regarded as white noise as the discharged CO_2 weight and ballast weight may not always be the same. Twenty simulated 4-hour extreme values are used to predict the maximum response of SST during hovering in extreme currents based on the ACER method. The ACER method proposed (Naess & Gaidai, 2009) is a Monte Carlo based modern extreme value prediction method that has been applied widely in engineering. The technique has been used mainly in naval architectures to estimate structural response (Gaidai, Storhaug, & Naess, 2016) (Xu, Ji, & Soares, 2019) and sea states, such as wind (Gaidai, et al., 2019), wave (Naess & Karpa, 2015), and current profiles (Yu, Wu, Xie, Wang, & Naess, 2020). The station keeping problem during the CO_2 offloading process is presented as a block diagram in Figure 2.3.

2 MODEL SET-UP AND IMPLEMENTATION

The SST dynamic Simulink model was introduced by Ma et al. (Ma, Da Silva, Xing, & Sui, 2022a), including a plant model, actuators and current. SST plant model has hydrodynamic forces due to added mass, hydrodynamic drag, and body lift. The actuator model consists of a propeller, thrusters, compensation tanks and hydroplanes; the ocean current model includes current velocity and direction, modelled as a stochastic process. The block diagram of the SST dynamic model is presented in 2.6 and shows the graphical representation.

2.1 SST Design Parameters

The most critical design parameters of the baseline SST design related to the offloading process modelling and analysis are included (Ma, Xing, Ong, & Hemmingsen, 2021). Table 2.1 presents the SST design parameters where the coordinate system in 2.2 is considered.

Table 2.1. SST Design Parameters.

[Variable]	[Value]	[Unit]
Total mass	[3.36×10^7]	[kg]
Pitch moment of inertia I_{yy}	[3.63×10^9]	[kg·m^2]
Maximum carbon dioxide capacity	[1.7×10^6]	[kg]
Length	[164]	[m]
Beam	[17]	[m]
Centre of buoyancy $[x_b, y_b, z_b]$	[0,0,-0.41]	[m]
Hydroplane position x_{hyd}	[67]	[m]
Bow, aft thruster thrust coefficient K_{Tt}	[0.4]	[-]
Propeller thrust coefficient K_{Tp}	[0.19]	[-]
Bow compensation tank location along SST length	[65.3]	[m]
Aft compensation tank location along SST length	[-65.3]	[m]
Bow, aft compensation tank volume	[800]	[m^3]
Cargo pump rate	[4000]	[m^3/h]
Ballast pump rate	[400]	[m^3/h]
Carbon dioxide capacity	[16,362]	[m^3]
Bow, aft thruster diameter d_t	[2]	[m]
Propeller diameter d_p	[7]	[m]
Hydroplane area A_{hyd}	[40]	[m^2]
Forward tunnel thruster position x_{tf}	[60]	[m]
Aft tunnel thruster position x_{ta}	[-60]	[m]

2.2 SST Coordinate System

As shown in Figure 2.1, the body-fixed coordinate system is situated at the SSTs centre of gravity, relative to a global earth-fixed coordinate system based on NED, North-East-Down. North-East-Down is defined relative to the earth's reference ellipsoid, i.e., the World Geodetic System (WGS 84), where the axes point towards true North, East and downward normal to the Earth's surface. WGS 84 is an ECEF (Earth Centred Earth Fixed) reference frame, which also utilises the latitude, longitude, and altitude coordinates.
For any stability related matters of submerged bodies, the two main terms are centre of buoyancy and centre of gravity. The centre of buoyancy, located at the centroid of the SST, is located slightly above the centre of gravity. The positive global surge motion x points to the bow direction, and positive heave motion z points downward, positive pitch motion θ points from z-axis to the x-axis; the velocities defined in the body frame are u, w, and q, respectively; the accelerations are $\dot{u}$, $\dot{w}$ and $\dot{q}$, correspondingly.

The maximum and minimum depth excursions are measured at 5 points, as illustrated in Figure 2.1. Point ① locates at the CoG of the SST, point ② locates at the aft top, point ③ locates at the bow top, point ④ locates at the aft bottom, and point ⑤ locates at the bow bottom of the SST.

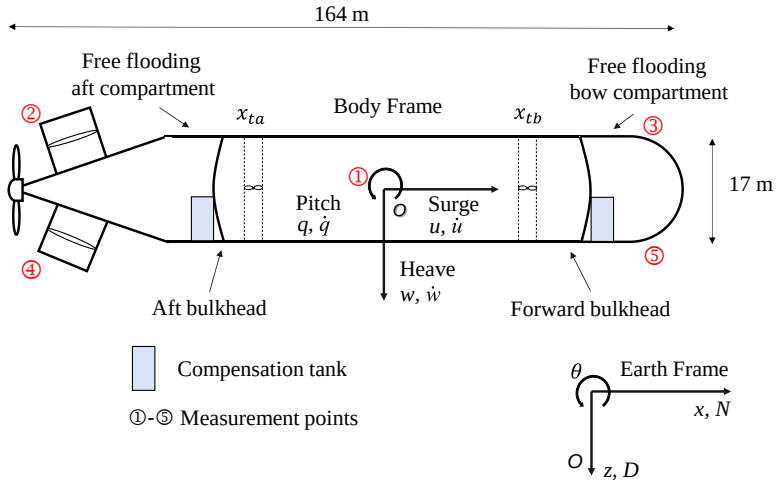

Figure 2.1. SST body frame and earth frame coordinate systems.

Table 2.2. SST velocity and acceleration notations.

[Variable]	[Notation]
Surge velocity (body frame)	u
Surge acceleration (body frame)	$\dot{u}$
Heave velocity (body frame)	w
Heave acceleration (body frame)	$\dot{w}$
Pitch velocity (body frame)	q
Pitch acceleration (body frame)	$\dot{q}$
Translational motion (global earth frame)	x
Translational motion (global earth frame)	z
Pitch rotational motion (global earth frame)	θ

2.3 SST Plant Model

To be able to understand the behaviour of the physical system, we introduce the equations (Eq. (3) and Eq. (4)) of motion of the SST. These consists of kinetic equations of motion and dynamic equations of motion. Written in vectorial form, they are expressed as:

$$\dot{\eta} = J_{\Theta}(\eta)\nu \qquad \text{Eq. (3)}$$

$$M\dot{\nu} + C(\nu)\nu + D(\nu)\nu + g(\eta) = \tau \qquad \text{Eq. (4)}$$

In the equations, η is SST motion in global coordinate; ν represents the velocity vector; $J_{\Theta}(\eta)$ is the matrix of Euler transformation; M is the matrix which contains the mass and added mass of the SST; $C(\nu)$ is a matrix containing the Coriolis-centripetal forces; $D(\nu)$ is a matrix consisting of the hydrodynamic drag forces; $g(\eta)$ is the vector for gravitational and hydrostatic forces; τ is the control force vector. Eq. (3) can be expanded as:

$$\underbrace{\begin{bmatrix}\dot{N}\\ \dot{D}\\ \dot{\theta}\end{bmatrix}}_{\dot{\eta}} = \underbrace{\begin{bmatrix}\cos\theta & \sin\theta & 0\\ -\sin\theta & \cos\theta & 0\\ 0 & 0 & 1\end{bmatrix}}_{J_{\Theta}(\eta)} \underbrace{\begin{bmatrix}u\\ w\\ q\end{bmatrix}}_{\nu} \qquad \text{Eq. (5)}$$

where the notations of the motions are illustrated in Figure 2.1.

The matrices in the dynamic equations of motion (Eq. (4)) can be expanded as follows:

$$M = \begin{bmatrix} m - X_{\dot{u}} & 0 & mz_g \\ 0 & m - Z_{\dot{w}} & -Z_{\dot{q}} \\ mz_g & M_{\dot{w}} & I_{yy} - M_{\dot{q}} \end{bmatrix} \quad \text{Eq. (6)}$$

$$C(\nu) = \begin{bmatrix} 0 & 0 & 0 \\ 0 & m - Z_{\dot{w}} & -(m - X_{\dot{u}})u \\ 0 & (Z_{\dot{w}} - X_{\dot{u}}) & 0 \end{bmatrix} \quad \text{Eq. (7)}$$

$$D(\nu) = \begin{bmatrix} X_{|u|u}|u| & X_{wq}q & X_{qq}q \\ Z_{uq}q & Z_{|w|w} + Z_{uw}u & Z_{q|q|} \\ M_{uw}w & M_{|w|w} & M_{uq}u + M_{|q|q} \end{bmatrix} \quad \text{Eq. (8)}$$

$X_{\dot{u}}$, $Z_{\dot{w}}$, $Z_{\dot{q}}$, $M_{\dot{w}}$, and $M_{\dot{q}}$ are added mass hydrodynamic coefficients.

$X_{|u|u}$, $Z_{|w|w}$, $Z_{|q|q}$, $M_{|w|w}$, and $M_{|q|q}$ are drag terms.

X_{wq}, X_{qq}, Z_{uw}, Z_{uq}, M_{uq} are cross-term added mass hydrodynamic coefficients.

Z_{uw} is the body lift and M_{uw} is the Munk moment.

The hydrodynamic derivatives used in this study are listed in Table 2.3.

Table 2.3. Hydrodynamic derivatives.

[Variable]	[Value]	[Unit]
$X_{\dot{u}}$	-5.14×10^5	kg
$Z_{\dot{w}}$	3.29×10^7	kg
$M_{\dot{w}}$	-4.40×10^8	kg·m
$Z_{\dot{q}}$	-4.40×10^8	kg·m
$Z_{|q|q}$	4.79×10^9	kg·m
$M_{|q|q}$	-4.34×10^{12}	kg·m^2
X_{wq}	-3.28×10^7	kg
X_{qq}	-4.40×10^8	kg·m

2.4 SST Actuator Model

The SST actuator model was initially developed by (Ma, Da Silva, Xing, & Sui, 2022a). Most fields within the marine guidance, navigation, and control (GNC) environment, e.g., collision avoidance and path following, depend on accurate dynamic models. The guidance relates to the desired trajectory (i.e., the desired path from one location to another, taking velocity, acceleration, and rotation into consideration). Navigation considers the vessel's location at a given time, and the distance travelled (e.g., internal measurement units can be used for tracking trajectory). Control deals with the execution of control measures such as thrusters, the propeller, hydroplanes, and ballast tanks, i.e., control of the desired movement at any given time.

To derive the equations of motion of the SST and describe its kinematics, the two reference frames (body frame and earth frame) are defined in 2.2.

2.4.1 Propeller

Propulsion and propeller design for submarines are mainly based on the mission requirements and areas of use. As most submarine propeller design is of military importance, a low acoustic signature is often of a high priority. This is not the case for the SST, and efficiency and thrust are the dominating parameters. During propeller design and selection, one of the first steps would be to confirm the number of blades. The fluctuating forces cause acoustic noise from the propeller blade on the propeller itself since the propeller is operating in the vessel's wake (Renilson, 2018). The flow into the propeller will affect both the propeller efficiency and acoustic performance. Parameters such as hull shape design and cone angle will govern the inflow characteristics.

The quasi-propulsive coefficient, denoted QPC, presents the proportion of usable power compared to the power delivered to the SST propeller (Renilson, 2018), and dictates the efficiency directly. This has been calculated and presented (Ma, Xing, Ong, & Hemmingsen, 2021) with a value of 0.97, which is relatively high. From the initial design of the SST, a three-bladed Wageningen B-series propeller was chosen (Bernistas, Ray, & Kinley, 1981). This blade configuration has a diameter of 7 m, an operating speed of 38 RPM and a blade ratio of 0.3. The propeller thrust coefficient K_{Tp} is given as 0.19. Propeller thrust force can be calculated using Eq. (4) where n_p is the rotational speed of the propeller and d_p is the blade diameter.

$\tau_p = K_{Tp} \cdot \rho \cdot {n_p}^2 \cdot {d_p}^4$	Eq. (9)

Utilising a large single-screw propeller together with a slow rotating speed provides high efficiency, and it also offers a small machine weight compared to a multiple propeller setup (Gabler, 1972). Parameters such as cavitation and friction must be considered during design, as they will affect both the integrity of the propeller blades and the total drag exerted on the vessel. As the single-propeller is situated at the aft centre of the SST, it will offer a higher efficiency compared to a twin-propeller setup due to the concentric wake and propulsion energy recovery. It has been shown (Gabler, 1972) that low rpm. single-screw propeller, with a low propeller load has higher propulsion efficiency than a twin-screw drive.

2.4.2 Hydroplanes

Hydroplanes have been designed on each side of the SST (ref. Figure 2.1), one hydroplane on the starboard side and one on the port side. The hydroplanes will adjust the depth of the SST and act as pitch control during CO_2 transportation. The lift force generated by the hydroplanes is formulated in Eq. (10), where ρ is density of sea water 1025 $\frac{kg}{m^3}$. The hydroplane area A_{hyd} is set to 40 m^2. The hydroplane lift rate coefficient C_L and the hydroplane angle δ_{hyd} has been set to 6.1 rad^{-1} and 0 deg., respectively. For this design, Bower's air foil profile has been utilised (Bowers, Murillo, Jensen, Eslinger, & Gelzer, 2016).

$\tau_{hyd} = 0.5 \cdot \rho \cdot C_L \cdot A_{hyd}(\delta_{hyd} - \theta)u^2$	Eq. (10)

2.4.3 Tunnel Thrusters

The SST utilises two tunnel thrusters (Ma, Da Silva, Xing, & Sui, 2022a) (Xing, Gaidai, Ma, Naess, & Wang, 2022), one in the front (x_{tf}) and one at the aft (x_{ta}), as presented in Figure 2.1. Tunnel thrusters are widely operated in the marine environment and are used for surface ships to provide low-speed manoeuvrability during berthing, deliver station keeping abilities as well as emergency steering when needed. For underwater vehicles, such as the SST, tunnel thrusters are mainly used for manoeuvring at low speeds and controlling the hydrostatic balance. Both SST thrusters are located 60 m in front and aft of the COB, respectively (Table 2.1). Calculation of forward thrust and backward thrust can be completed using Eq. (11), where the thrust coefficient $K_{Tt} = 0.4$, d_t is thruster diameter and n_t is the rotational speed of the thruster.

$F_T = K_{Tt} \cdot \rho \cdot n_t \cdot \lvert n_t \rvert \cdot d_t^4$	Eq. (11)

An estimation of thruster diameter of 2 m where the Kongsberg Marine tunnel thruster specifications have been used (Kongsberg, 2019). The thruster vector τ_T consisting of the propeller and thrusters' contributions in the surge, heave, and pitch can be summarised as:

$$\boldsymbol{\tau_T} = \begin{bmatrix} F_P \\ F_{Tb} + F_{Ta} \\ F_{Tb}x_{Tb} + F_{Ta}x_{Ta} \end{bmatrix}$$	Eq. (12)

where F_{Tb} and F_{Ta} as calculated by Eq. (11), are thrusts from the bow and aft thruster, respectively.

2.4.4 Ballast Tanks

To ensure the SST is neutrally buoyant and trim, two ballast tanks have been designed. One ballast tank at the front and one ballast tank at the aft of the SST (Figure 1.7), each one placed 70 m in front and the aft of the centre of gravity. The two tanks combined have a total mass of 1469,000 kg in the model. The weights are included in the total mass of the SST. The utilisation of the ballast thanks will vary between the different hydrostatic load cases: submerged and CO_2 filled; submerged and seawater filled; surfaced and CO_2 filled; surfaced and seawater filled.

2.5 Ocean Current

Ocean current is non-linear and changes with time and location. Numerous research papers and guidelines have introduced the modelling of stationary current (DNV, 2010), (Domps, Dumas, & Marmain, 2021), (Yu, Wu, Xie, Wang, & Naess, 2020)). However, these models are not sufficient to study the positioning problem of the SST subjected to time-varying current. The model of the ocean current (current profile is described in Eq. (13) and Eq. (14)) introduced by Fossen and Sorensen (Fossen, 2011) (Sorensen, 2018) has been used for the simulations and calculations performed in this thesis.

$$\dot{V}_c + \mu_1 V_c = \omega_1$$	Eq. (13)

$$\dot{\theta}_c + \mu_2 \theta_c = \omega_2$$	Eq. (14)

The direction and velocity of the ocean current model have been described as a first-order Gauss-Markov process, meaning the model satisfies the requirements for both the Gaussian and Markov processes, respectively. V_c represents the current speed, μ_1 and μ_2 relates to the time constants of the process, θ_c is the inflow angle of the current relative to the SST and ω_1 and ω_2 are white noise from the Gaussian process.

The constants μ_1 and μ_2 will influence the rise time of the steady state, i.e., the time it takes before a steady state is obtained and should be nonnegative (Fossen, 2011). To exemplify, the time constants are set to be 1 in this work. The noise power of the Gaussian white noise is set to 0.1 when rendering the turbulency of the inflow.

For 2D irrotational current, the current velocity in the global frame can be expressed as:

$$\boldsymbol{v_c^g} = \begin{bmatrix} V_c \cos\theta_c \\ V_c \sin\theta_c \\ 0 \end{bmatrix} \quad \text{Eq. (15)}$$

Therefore, the current velocity described in the SST body frame can be expressed as:

$$\boldsymbol{v_c^b} = \begin{bmatrix} V_c \cos(\theta_c - \theta) \\ -V_c \sin(\theta_c - \theta) \\ 0 \end{bmatrix} \quad \text{Eq. (16)}$$

Finally, the relative velocity is obtained by summing up v_c^b and $\dot{\eta}$. Current data in the North Sea is used as the baseline as SST is designed to be deployed in the Norwegian sector. Extreme current velocity is determined based on the work conducted by (Pugh, 1982), which estimated the extreme current distributions and velocities by applying joint tide-surge probability techniques to the observation data in Inner Dowsing, North Sea. The extreme current prediction result is summarised in Figure 2.2. The maximum current velocity is observed at the South-West 165 ° direction. The corresponding extreme current speed is 1.6 m/s with a 50-year return period.

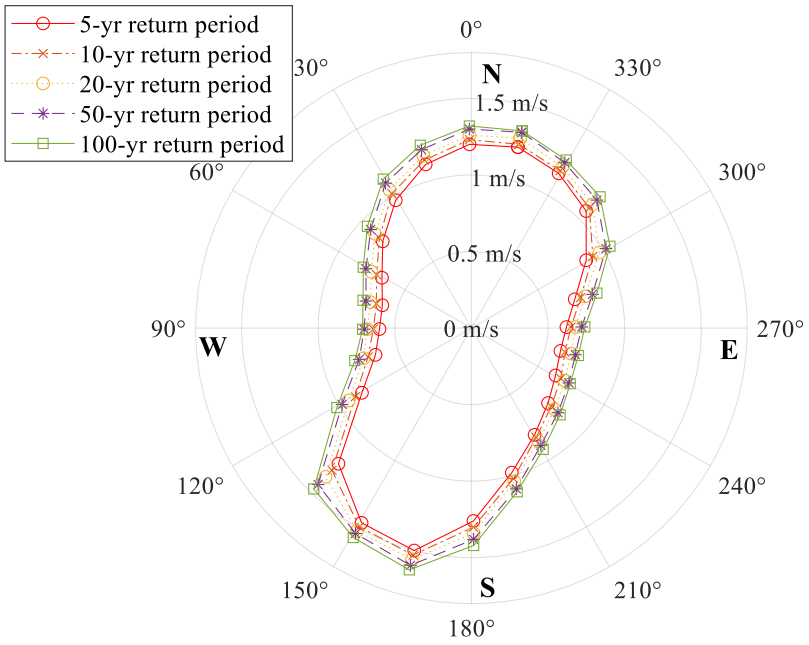

Figure 2.2. Extreme current velocity distribution at Inner Dowsing **(Pugh, 1982)**.

Extreme currents above 1.6 m/s are introduced in this study and are located in the global coordinate system. For calculating the hydrodynamic forces, the current speed has been transformed into a body-fixed coordinate system for the SST and added to the movement velocity.

2.6 Simulink Modelling

The physical system of the SST with its associated dynamic properties and constraints has been modelled in three separate blocks in Matlab/Simulink. The *water current* is modelled in a designated block and added to the SST velocity. This gives us the relative velocity, linking the SST and the medium.

The *plant model* contains the SST equations of motion, i.e., the body lift force, added mass and the damping. Propeller, thrusters, ballast tanks, hydroplanes, and associated inputs have been modelled in the *actuator* block. The block diagram representation of the SST model is displayed in Figure 2.3.

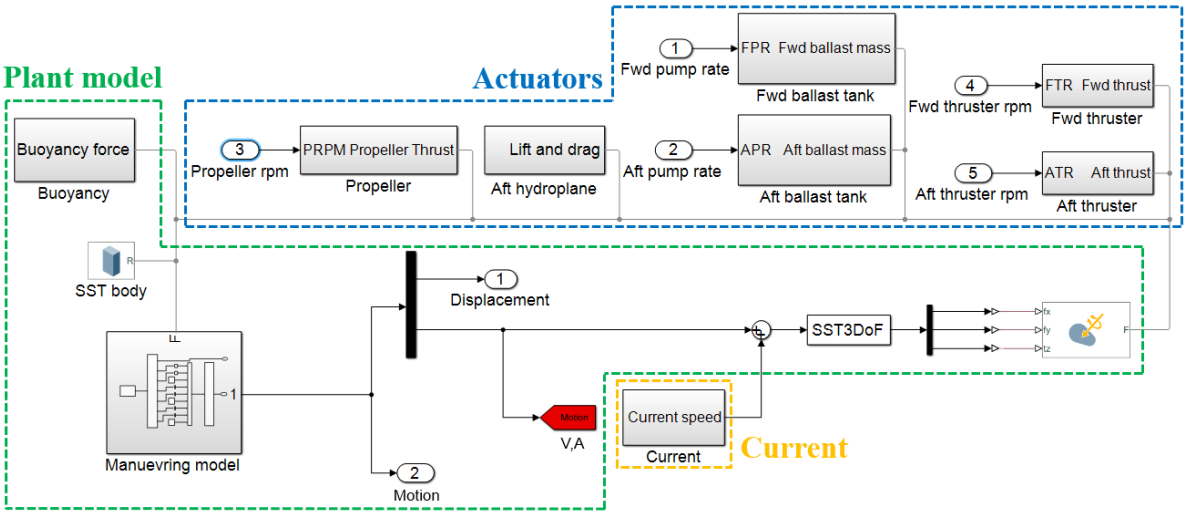

Figure 2.3. Block diagram representation in Simulink.

3 LQR DESIGN

In control theory problems, we investigate challenges within the control theory of linear or nonlinear dynamic systems. The linear dynamic systems follow the superposition principle and deal with models where the change in output is more or less proportional to its input. Linear systems are found in many applications, such as signal processing, communication, economics, and automatic control systems. The nonlinear systems are more complex, and the obtained output from the dynamic model is not proportional to the change of model input. As nearly all problems are, by nature, inherently nonlinear, the changes over time may seem unpredictable and chaotic (e.g., weather predictions). Nonlinear systems are challenging to solve because of dependencies on the system variables related to each other. Most engineering problems involving nonlinear dynamic systems are linearized to get a close approximation solution. This linearization results obtain an approximate result at a lower work/cost, time, and effort.

Motion control systems within the marine environment are often designed using PID control methods (Fossen, 2011). The model-based control systems are a visual and mathematically designed method based on the dynamic systems. These control systems are used for various autopilot designs, position mooring systems, station keeping and line-of-sight control systems, to mention a few. These approaches are also commonly used within other industries such as aerospace, automotive applications, and industrial machines.
The dynamic system of the SST is both nonlinear and coupled through the surge, heave, and pitch motion, respectively.

As the name indicates, the linear quadratic regulator can only be implemented for *linear* dynamic systems. The nonlinear dynamics of the SST must be linearized at steady points/equilibrium points to determine the controller gains at these respective points.
Linear quadratic regulators provide optimal control feedback, where the gains are used to provide a high performance of the dynamic system.

The control system, initially designed by (Ma, Da Silva, Xing, & Sui, 2022a) and extended by (Xing, Gaidai, Ma, Naess, & Wang, 2022), for the hovering of the SST during offloading is presented in Figure 3.1, by its closed control loop. The control input u from the actuator block is calculated from the state feedback and the trajectory reference. The optimal gain matrix K for the system is determined based on the defined performance and effort parameters. Defining the performance and effort parameters will be influenced by the desired properties of the SST.

E.g., one specific gain matrix can be determined by imposing importance on the stability of the SST under the offloading process (i.e., minimal movement is required). This would increase actuator efforts and reduce the energy storage and SST range at a higher rate.
On the other hand, if the design of the SST would present more flexibility in the movement during offloading, we would penalise actuator effort to reduce the energy consumption during the offloading process. This would again give us a different gain matrix, K.

3.1 Linear State-Space Model

State-space representations of physical, dynamic systems are mathematical models (in this case, modelled in Matlab) containing state variables, inputs, and outputs in discrete or continuous time. The dynamic system is represented by differential equations, and the system variables are *state variables* which are dependent on the values they have at the particular moment of time they are assessed and evaluated. Both the controllability and the observability conditions must be fulfilled, and both these concepts have played significant roles in the development of modern control theory. The controllability is met if:

$rank\,[B \quad AB \quad A^2B \quad \dots \quad A^{n-1}B] = n$	Eq. (17)

where rank represents the number of linearly independent rows in a matrix. n represents the number of state variables in the system. It concerns whether the control input can steer the states to required locations in the state space.

System observability relates to the internal states and how well these are evaluated based on the dynamic system output. A system is said to be observable (Fossen, 2011) if the current states can be determined using only the systems' outputs and are applicable for any possible sequence in the finite time domain.

3.1.1 Linear State-Space Function

The SST model is highly coupled, nonlinear, and time-variant and linear quadratic regulator (LQR) is a technique for obtaining an optimal control based on state-space representation. The linear state-space equations for the SST are presented in Eq. (18) (state equation), and Eq. (19) (output equation), where x represents the state of the system (state vector), and y represents the output of the system (output vector). Matrix A is the system's dynamics, and vector u represents the control input. B and C are input and output (sensor) matrices, respectively.

$\dot{x} = Ax + Bu$	Eq. (18)

$y = Cx$	Eq. (19)

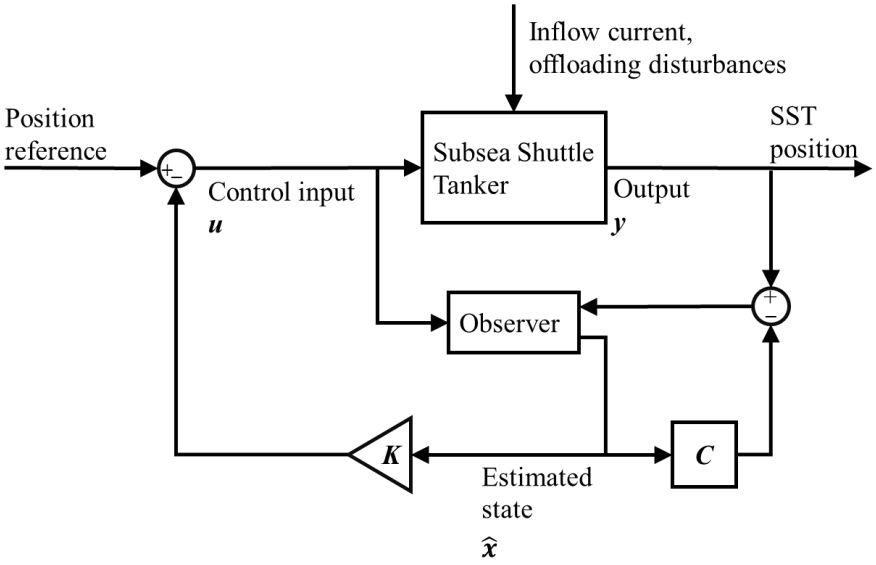

Figure 3.1. SST control block diagram.

3.1.2 Model Linearization

The SST manoeuvring is by nature dynamic, nonlinear, and coupled. It can be seen as a nonlinear mass-damper-spring-system (Fossen, 2011) which will be transformed into linear equations.

By linearising the model, we can attain the linear space-state function.

- Input of linearised model, $u = [n_{tb}; n_p; n_{ta}]$
- Output of linearised model, $y = [N; D; \theta]$
- Obtained state vector, $x = [N; D; \theta; \dot{N}; \dot{D}; \dot{\theta}]$

The linearisation is a linear approximation of the nonlinear system and will only be valid in a small region around the chosen operating points. The relevant operating points for the linearisation of the manoeuvring model are specified as 1 m/s design current speed with an inflow angle of 1°. A, B and C are shown to be 6 × 6, 6 × 3, and 3 × 6 matrices, respectively.

$$A = \begin{bmatrix} 0 & 0 & 0 & 1 & 0 & 0 \\ 0 & 0 & 0 & 0 & 1 & 0 \\ 0 & 0 & 0 & 0 & 0 & 1 \\ 0 & 0 & 2.65 \times 10^{-5} & 1.00 \times 10^{-3} & -1.21 \times 10^{-4} & -1.45 \times 10^{-2} \\ 0 & 0 & 2.87 \times 10^{-6} & -1.32 \times 10^{-4} & -8.91 \times 10^{-3} & 5.18 \times 10^{-2} \\ 0 & 0 & -2.37 \times 10^{-2} & 6.21 \times 10^{-5} & 3.87 \times 10^{-3} & -5.96 \times 10^{-2} \end{bmatrix} \quad \text{Eq. (20)}$$

$$B = \begin{bmatrix} 0 & 0 & 0 \\ 0 & 0 & 0 \\ 0 & 0 & 0 \\ 2.54 \times 10^{-10} & -8.80 \times 10^{-5} & -4.24 \times 10^{-10} \\ 3.84 \times 10^{-6} & -5.25 \times 10^{-9} & 6.40 \times 10^{-6} \\ 7.13 \times 10^{-7} & 0 & -1.19 \times 10^{-6} \end{bmatrix} \quad \text{Eq. (21)}$$

$$C = \begin{bmatrix} 1 & 0 & 0 & 0 & 0 & 0 \\ 0 & 1 & 0 & 0 & 0 & 0 \\ 0 & 0 & 1 & 0 & 0 & 0 \end{bmatrix} \quad \text{Eq. (22)}$$

3.2 Linear Quadratic Regulator

In control theory, the focus is often to obtain and design the desired control law where we optimize a performance index (Kumar & Jain, 2019), i.e., maximize or minimize based on our cost function target. As the name implies, the linear quadratic regulator requires a linear system. The linear time-invariant system (Eq. (18) and Eq. (19)) has constraints of linearity and time-invariance, i.e., the change in output is linear with the change of input and regardless of if we make these changes after time T or time $T + n$. The output will be the same and the only difference will be the time delay n.

As the LQR is an optimal control, it aims to solve the optimisation problem at hand, i.e., performance versus effort, and thereby find the gain matrix K. For the time-invariant system expressed in Eq. (18) and Eq. (19), the LQR solves the quadratic weighted cost functions and approaches the optimal gain based on our weighted performance and effort (Fossen, 2011). Eq. (23) shows the minimised quadratic cost function, where Q represents the performance and R represents the effort.

$L(x,u) = \int_0^\infty (x^T Q x + u^T R u) dt$	Eq. (23)

The state weighting matrix is defined as $Q = Q^T \geq 0$, and the energy weighting matrix for the actuator is defined as $R = R^T \geq 0$. These weighting matrices give us the importance of the state error together with the power consumption of the actuator system.
By differentiating between the initial state of the system and the desired state of the system, we can penalise the different states and efforts, i.e., adjusting the diagonal elements in the matrix Q and R, respectively. By doing this, we can obtain the most optimal solution based on our relative weights of the performance and effort.
The control law for LQR is obtained by solving the LQR problem and is described in Eq. (24).

$u = -Kx$	Eq. (24)

The gain matrix K is a 3×6 matrix derived from the optimisation problem.
When designing the linear quadratic regulator, the controllability of the SST must be satisfied. The linear state matrix and linear input matrix, A and B, must be controllable for the planar

model. The controllability matrix Con must have full rank (i.e., its rank, number of linearly independent rows equals the largest possible for the matrices of the same dimensions) and must thus have a right inverse.

$Con = [B\|AB\|\cdots\|A^{n-1}B]$	Eq. (25)

Eq. (25) shows the controllability matrix for the SST planar model, and the linearized model displays a controllability matrix of 6, i.e., controllable.

3.3 Observer

As Figure 3.1 displays, a Luenberger observer (Luenberger, 1972), also known as a state observer or state estimator, is included in the block diagram for monitoring the system states. By representing sensors, the Luenberger observer is a system that estimates the internal state of the SST. The variables denoted with " ˆ "are generally associated with the observer. This is to distinguish them from the physical system equation variables.

The Luenberger Observer block in Matlab uses the backward Euler method for numerically solving the ordinary differential equations. Understanding and knowing the system states are required for most control theory problems. The challenge described in this thesis focus on stability problems, but observer theory is also used in other applications such as, e.g., dynamic state estimation in power systems (Anagnostou, Boem, Kuenzel, Pal, & Parisini, 2018). Predicting the internal states of the physical SST system during offloading is critical for the design of the motion controller. The estimated state $\hat{x}$ is based on the control input u and the system output y. The system is assumed to be observable, and u and y can thus construct the system's state in a finite time interval.
The observer is mathematically modelled as per. Eq. (26).

$\dot{\hat{x}} = A\hat{x} + Bu + K_L(y - \hat{y})$	Eq. (26)

K_L represents the observer gain and $\hat{y}$ is an estimation of the output vector y and $(y - \hat{y})$ is the error, or correction term, i.e., the difference between the estimated and actual outputs. The observer has the same dynamics as the system, but it has the additional error term. The close loop poles are placed on the negative side of the real axis to achieve the observer gain.
The observer gain sensitivity analysis was performed by (Ma, Da Silva, Xing, & Sui, 2022a), which shows the observer performance increases with moving the pole position further to the

negative axis. Same with (Ma, Da Silva, Xing, & Sui, 2022a), the pole position of p=[-4;-4;-4;-2;-2;-2] is used in this work.

Similarly, the system needs to be observable before implementing the Luenberger observer; the observability matrix in Eq. (27) of the SST has a full column 6.

$Obs = [C^\top \vert A^\top C^\top \vert \cdots \vert (A^\top)^{n-1} C^\top\ ]$	Eq. (27)

4 ACER

The average conditional exceedance rate (ACER) is used in extreme value predictions and distributions, and the method was introduced by (Naess & Moan, Stochastic dynamics of marine structures, 2013). This extreme value prediction is made by constructing a series of non-parametric functions which are not based on asymptotic sample theory. The method has been applied for stationary and nonstationary stochastic processes and includes all global maximum peaks. It also avoids the necessity of declustering of data to ensure independence (Karpa 2015). From (Xing, Gaidai, Ma, Naess, & Wang, 2022), it was manifested that the extreme responses were twice as high for a 5-year return period compared to the maxima of a 4-hour response period.

For response processes of marine structures, the Gumbel distribution would almost always be the appropriate one (Naess & Moan, 2013). Compared to other extreme value estimation techniques such as generalised extreme value distribution and peaks-over-threshold method, ACER does not require the observations to be independent and identical distributed, i.e., each random variable will have the same probability distribution as the other random variables. No outcome will influence other outcomes (independent), and all samples come from the same distribution (identical). The non-parametric functions based on ACER functions of various orders are developed, and the aim is to approximate the actual extreme value distribution.
In detail, the ACER method determines the distribution function of the extreme value, which is denoted $M_N = max\{X_j;\ j = 1,\ \cdots,\ N\}$. An accurate estimation of $P_\eta = Prob(M_N \leq \eta)$ is wanted for large values of η. It denotes the probability of the occurrence of the extreme value η, and it follows:

$P_\eta = Prob(M_N \leq \eta) = Prob(X_1 \leq \eta,\ \cdots,\ X_N \leq \eta)$	Eq. (28)

Solving this equation, a succession of conditional approximation $P_k(\eta)$ is used, where $P_k(\eta)$ tends to approach to P_η as k increases. For $N \gg 1$ and $k = 1,2,\cdots$, $P_k(\eta)$ is represented as (Naess & Gaidai, 2009):

$P_k(\eta) \approx exp(-\sum_{j=k}^{N} \alpha_{kj}(\eta))$	Eq. (29)

where $\alpha_{kj}(\eta) = Prob\left(X_1 > \eta | X_{j-1} \ll \eta, \cdots, X_{j-k+1} \leq \eta\right)$ and it represents the exceedance probability (only counted if proceeded by non-exceedances). The notion of average conditional exceedance rate is described in Eq. (30) will be calculated as follows:

$\varepsilon_k(\eta) = \frac{1}{N-k+1}\sum_{j=k}^{N} \alpha_{kj}(\eta), k = 1,2,\cdots$	Eq. (30)

where N represents the number of sample points for a specific moment X_n. Onwards, for $k \geq 2$, $\tilde{\varepsilon}_k(\eta)$ is used instead of $\varepsilon_k(\eta)$. This is done because it is easier to use for nonstationary or long-term statistics (Naess & Moan, Stochastic dynamics of marine structures, 2013), and it is defined as:

$\tilde{\varepsilon}_k(\eta) = \lim_{N\to\infty} \frac{\sum_{j=k}^{N} a_{kj}(\eta)}{N-k+1}$	Eq. (31)

$\lim_{N\to\infty} \frac{\tilde{\varepsilon}_k(\eta)}{\varepsilon_k(\eta)} = 1.$	Eq. (32)

where $a_{kj}(\eta)$ are the realised values for the observed time series, and Eq. (32) needs to be fulfilled. The ACER (for both stationary and nonstationary time series) sample estimate can be denoted as:

$\hat{\varepsilon}_k(\eta) = \frac{1}{R}\sum_{r=1}^{R} \hat{\varepsilon}_k{}^{(r)}(\eta)$	Eq. (33)

where R is the number of samples or realizations, and

$\hat{\varepsilon}_k{}^{(r)}(\eta) = \frac{\sum_{j=k}^{N} a_{kj}{}^{(r)}(\eta)}{N-k+1}$	Eq. (34)

where r denotes the specific realisation number.

With sufficient numbers of realizations and assumed independence, then the 95% confidence interval (CI) for the $\varepsilon_k(\eta)$ can be estimated as:

$CI(\eta) = \hat{\varepsilon}_k(\eta) \pm \frac{1.96\hat{s}_k(\eta)}{\sqrt{R}}$	Eq. (35)

where $\hat{s}_k(\eta)$ refers to the sample standard deviation of samples and can be estimated by:

$\hat{s}_k(\eta)^2 = \frac{1}{R-1}\sum_{r=1}^{R}(\hat{\varepsilon}_k^{(r)}(\eta) - \hat{\varepsilon}_k(\eta))^2$	Eq. (36)

The above equations for estimation of average exceedance rate are based on direct numerical simulations. In contrast, an extrapolation technique can reduce the computational time. Assuming the mean exceedance rate in the tail behaves similarly to $exp\{-a(\eta-b)^c\}$ $(\eta \geq \eta_0 \geq b)$ where a, b, and c are suitable constants. The ACER will therefore be assumed by:

$\varepsilon_k(\eta) \approx q_k(\eta) exp\{-a_k(\eta-b_k)^{c_k}\}$	Eq. (37)

where $\eta \geq \eta_1 \geq b_k$ and the function $q_k(\eta)$ varies slowly compared to the exponential function $exp\{-a_k(\eta-b_k)^{c_k}\}$ in the tail region. Continuously, this can be replaced by a constant for a fitting choice of the tail marker η_0. In the end, the Levenberg-Marquardt least-squares optimization method can be used to determine the constants $a_k, b_k, c_k \; and \; q_k$. (Naess & Gaidai, 2009) expressed their experience that this damped least-squares method is well suited for this assignment. (Chai, Leira, & Naess, 2018) concluded that the extrapolation scheme applied to capture the tail behaviour of the ACER functions was satisfactory for the extreme value predictions.

5 RESULTS AND DISCUSSION

5.1 Time Domain Response

In total, an 80-hour realisation consists of 20 independent 4-hour simulations performed in Simulink. Figure 5.1 exemplifies a 500 s stochastic current realisation. The mean current velocity is set to be 1.6 m/s while the mean inflow angle is 0 °. Correspondingly, Figure 5.2 exemplifies the response of the SST, i.e., SST state vector $x = [N; D; \theta; \dot{N}; \dot{D}; \dot{\theta}]$, in the global coordinate system to present the performance of the controller and the observer. Both measured states and actual states are presented. As shown in Figure 5.2 (a), the observer can provide excellent measurement for surge, heave, and pitch displacement of the SST; as shown in Figure 5.2 (b), the observed values for surge, heave, and pitch velocities are close to the actual velocities of the SST. In the presented time series, the SST has a steady surge off-site of approximately 1.2 m with a fluctuation amplitude of about 0.2 m. On the contrary, the heave motion of the SST has an amplitude of approximately 2 metres, significantly larger than the surge. This is caused by the giant side-way drag force. The pitch motion of the SST in the presented case is lower than 0.04 rad. As the SST has a length of 164 m, this can still result in an over 2 meter off-site to the bow and aft.

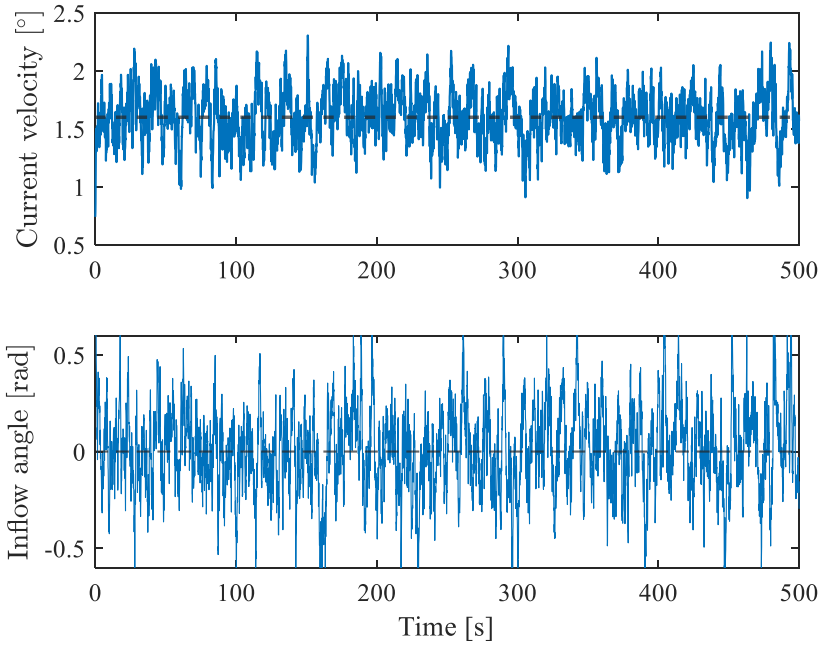

Figure 5.1. Exemplified current realization.

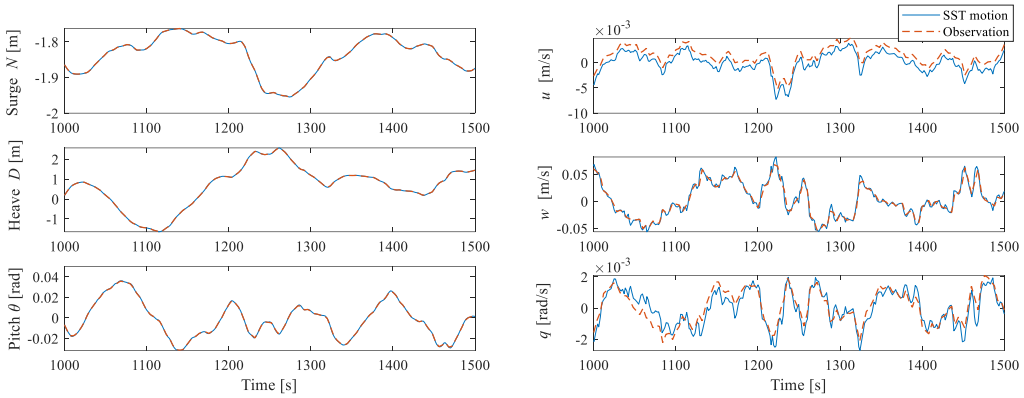

(a) **(b)**

Figure 5.2. SST response in 500 s realisation. (a) SST motion. (b) SST velocity.

From the SST time series, the responses of the five measurement points (Figure 2.1) are obtained. The maximum and minimum depth excursions in the 20 realisations for the five points are presented in Figure 5.3 (a) and Figure 5.3 (b), respectively. These are the inherent values to study the depth excursions of the SST and further predict the long-term extreme depth off-site of the SST, which helps determine the values bringing a cost-efficient design. Essentially, the extreme depth excursions happen at the bow and aft of the vessel, rather than the positions close to the mid-vessel, as the motions at those positions have a contribution from the pitch motion. Therefore, the minimum depth excursions are expected at the bow and aft of the upper bound of the SST, i.e., Point 3 and Point 2, as shown in Figure 5.3 (b). While the maximum depth is reached by the bow and aft of the lower bound, i.e., Point 4 and Point 5, measurement point 1 locates at the centroid of the SST and is provided as a reference.

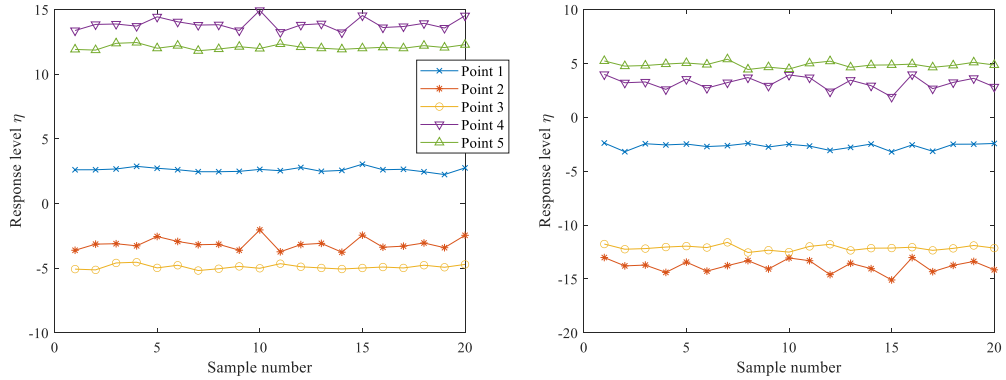

(a) **(b)**

Figure 5.3. (a) Maximum depth excursion. (b) Minimum depth excursion.

5.2 k Value Section

As mentioned in section 4 and by (Naess & Gaidai, 2009), the cascade of conditioning approximations $P_k(\eta)$ converge toward $P(\eta)$ when k increases. k value from 1-6 is checked in this study. The result for Point 4 maximum depth excursion is presented, for instance, in Figure 5.4. It can be noticed that for k from 1 to 6; the response η is at the same level. However, with the same $ACER_k(\eta)$, η is more conservative (larger) for $k = 1$ while the values for $k \geq 2$ are very close. Therefore, it is concluded that applying $k = 2$ returns to an accurate prediction of the SST extreme depth excursion for the measured points.

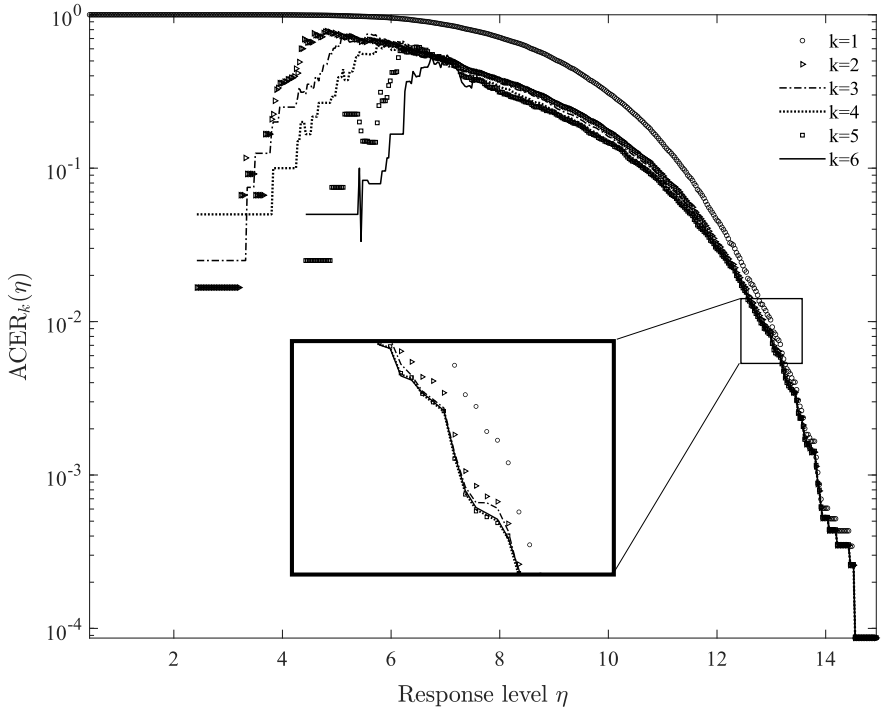

Figure 5.4. ACER functions for maximum depth excursion. Point 4 with different k values.

5.3 Extreme Depth Excursion Predicted by ACER Method

The extreme depth excursions of the SST measurement points using the ACER method for the 80-hour simulations are discussed in this section. Figure 5.5 and Figure 5.6 presents the extrapolation result with an exceedance rate of 1×10^{-6} of the minimum and maximum depth excursion, respectively. The 95 % confidence interval (CI) is presented in a dashed line, and the fitted 95 % CI are presented in a dotted line. A close fit to the simulation results can be observed for the ACER method.

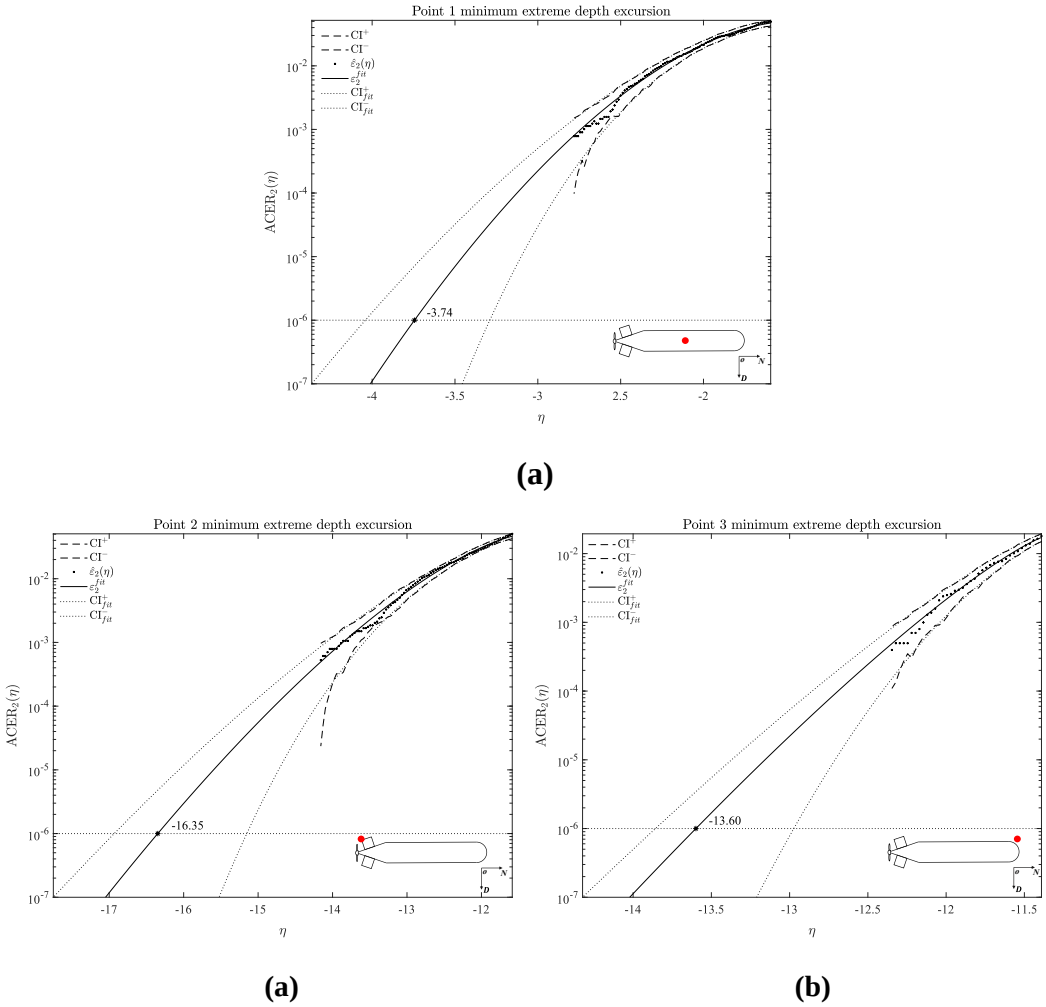

Figure 5.5. ACER extrapolation for maximum depth excursion, Points 1,2 and 3.

The minimum extreme response of the SST is observed at Point 2, as shown in Figure 5.5 (b)). The value with a 1×10^{-6} exceedance rate is -16.35 m from the reference offloading position, 2.75 m above the value for the SST bow. As a reference, this extreme value for the SST centroid (Point 1) is -3.74 m. The results indicate that if the SST offloads at 40 m safety depth, the minimum extreme depth excursion is 23.65 m (upper bound).

The maximum positive off-site (lower bound) is also observed at the aft (Point 4). Its value is 15.98 m, slightly lower than the absolute minimum depth excursion (16.35 m). The maximum extreme depth at the SST bow (Point 5) is 2.32 m smaller. As a reference, the maximum extreme off-site for Point 1 is 3.74 m, the same as the absolute minimum extreme. Therefore, when the SST is offloading at a 70 m water depth, the maximum depth excursion of the SST with a 1×10^{-6} exceedance rate is 86 m.

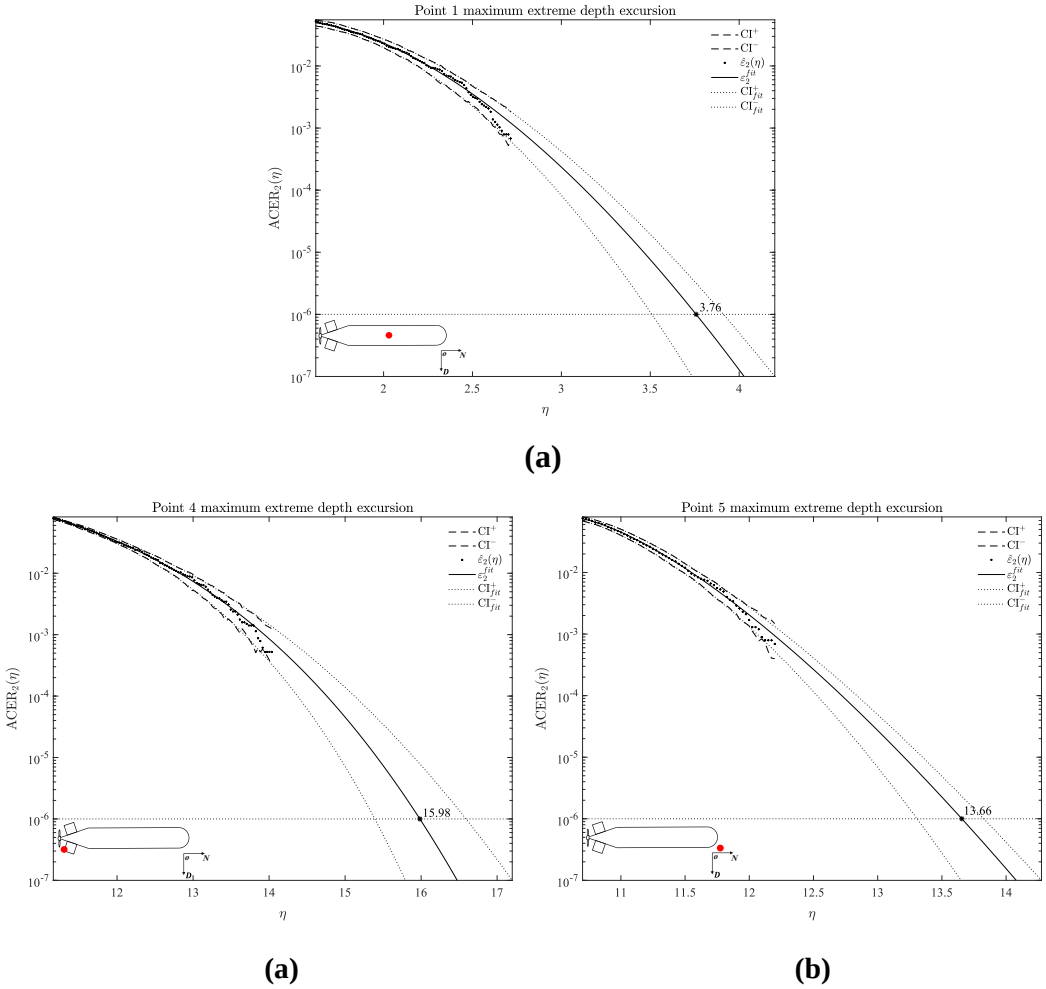

Figure 5.6. ACER extrapolation for maximum depth excursion. Points 1,4, and 5.

Finally, the ACER prediction results are summarised in Table 5.1, where 95% CI is stated in the parentheses. The main findings in this paper are denoted in Figure 5.7. The SST's permissible offloading depth region is between 40 m safety and 70 m nominal diving depth. However, under a 1.6 m/s extreme current condition, the maximum depth excursion can reach 86 m while the minimum extreme depth is 23.65 m. From the design perspective, it can be noticed that the maximum depth excursion is far from the 190 m collapse diving depth. This indicates that the guidelines are over-conservative in terms of defining the collapse pressure of the SST. With a better understanding of the SST, this value can be largely reduced. From the operation perspective, the SST should offload at least 16 m above the upper bound of any subsea installations in order to reduce the risk of collision. Also, the maximum draught of any surface/floating installations should be smaller than 23 m, i.e., the minimum depth excursion when the SST is offloading at the minimum allowable operation depth in the region of SST operation. Similarly, when an SST is offloading in fields with large draught floating structures, a 16 m minimum safety depth distance should always be maintained.

Table 5.1. Extreme value using the ACER method for an exceedance rate of 1×10^{-6}.

[Extreme Depth]	[Measurement Point]	[Extrapolation Value]	[95% CI^{-}]	[95% CI^{+}]
Minimum Depth	Point 1	-3.74431	-3.28976	-4.04082
	Point 2	-16.3476	-15.1519	-16.9326
	Point 3	-13.5987	-12.9733	-13.8570
Maximum Depth	Point 1	3.75786	3.50877	3.91145
	Point 4	15.9833	15.3909	16.5901
	Point 5	13.6554	13.3068	13.8259

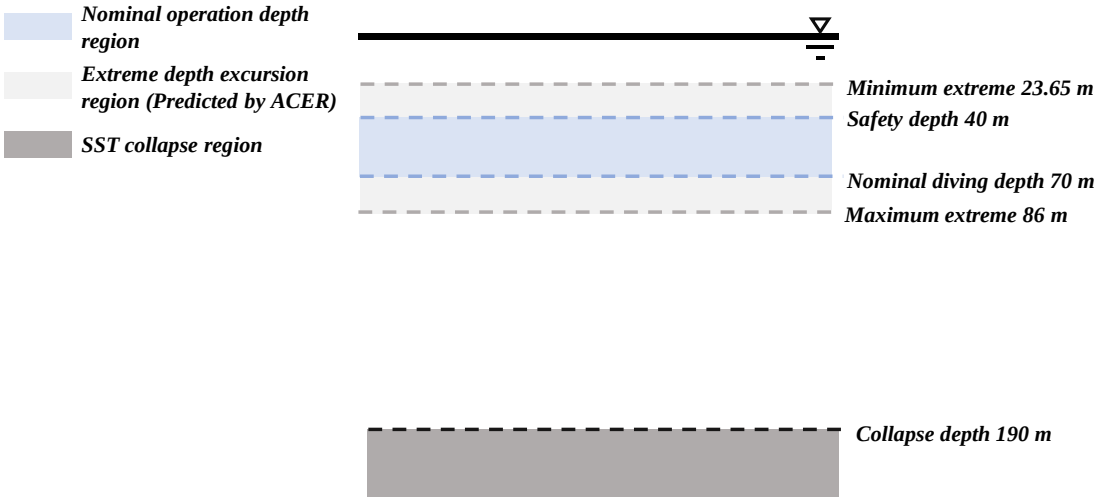

Figure 5.7. Depth region of SST offloading.

6 CONCLUSION

A novel autonomous subsea shuttle tanker concept was proposed as a cost-effective method of transporting liquid CO2 from shore & offshore facilities to subsea wells for enhanced oil recovery or permanent storage. However, the design of such a large autonomous underwater vehicle has not been detailed investigated. The current existing engineering codes tend to be very conservative by requiring a significant safety factor which will further result in a heavy structural design. Therefore, knowing the maximum response of the SST will benefit the study of such merchant underwater vehicles in two ways: first, knowing the extreme depth excursion unveils the maximum potential off-site of the SST during offloading. This reduces the level of uncertainty and denotes a less conservative design by knocking down the safety factor of the structural design. In addition, the extreme depth excursion can also provide a basis for the decision-makers in terms of SST operation. This study clarifies the maximum and minimum off-site of the SST from its desired offloading reference point and determines the required minimum safety distance from subsea installations and floating structures during offloading.

In this paper, the extreme response of the SST hovering during offloading is studied. Firstly, a 2D planar model is presented based on the baseline design configurations. The model consists of a rigid SST hull model that considers the hydrodynamic loads acting on the body, the main propeller and two tunnel thrusters located at the front and the aft to keep it stationary under incoming stochastic current. The time-variant stochastic current is described by a first-order Gauss-Markov process. The mean current velocity is set to be 1.6 m/s, corresponding to observation data in the North Sea with a return period of 50 years. Later, the SST planar model is streamlined to a linear state-space representation to obtain the controller gain and observer design. During the time-domain simulation, the SST's motion was first measured by the designed Luenberger observer and then passed to the LQR to calculate control inputs. 20 4-hour simulations are performed to get the SST response. Then, the extreme responses with the exceedance rate of 1×10^{-6} from 5 measurement points located at the SST centroid, upper-aft, upper-bow, lower-aft, and lower-bow, are studied using the ACER method. The main findings are summarised as follows:

- The effect of k value from 1 to 6 is studied, and the result shows that $k \geq 2$ can provide a very accurate prediction of the SST extreme response during hovering.

- The collapse design of the SST proposed by DNVGL-RU-NAVAL-Pt4Ch1 is very conservative for the SST. The extreme depth excursion happens at the SST aft during hovering. The maximum depth excursion is 86 m. This means the 19 bar (corresponds to 190 m water depth) collapse pressure can be significantly reduced.
- From an operational perspective, a minimum 16 m safety distance is suggested for the SST hovering. The SST should stay away from any subsea or floating structures with a minimum 16 m distance to avoid collisions.
- When the SST is offloading at a 40 m safety depth, the maximum draught of the floating structures in the vicinity should be less than 23 m.

7 REFERENCES

Anagnostou, G., Boem, F., Kuenzel, S., Pal, B., & Parisini, T. (2018). Observer-Based Anomaly Detection of Synchronous Generators for Power Systems Monitoring. *IEEE Transactions on Power Systems*.

ASME. (2022, April). *Drake Oil Well*. Retrieved from https://www.asme.org/about-asme/engineering-history/landmarks/40-drake-oil-well

Bai, Y., & Bai, Q. (2018). *Subsea Engineering Handbook.* Cambridge, MA: Gulf Professional Publishing.

Bernistas, M., Ray, D., & Kinley, P. (1981). *KT, KQ and Efficiency Curves for the Wageningen B-Series Propellers.* University of Michigan.

Bowers, A., Murillo, O., Jensen, R., Eslinger, B., & Gelzer, C. (2016). *On wings of the minimum induced drag: spanload implications for aircraft and.* Edwards, California: NASA.

bp. (2022). *Energy Outlook.* bp.

Chai, W., Leira, B., & Naess, A. (2018). Probabilistic methods for estimation of the extreme value statistics of ship ice loads. *Cold Regions Science and Technology.146:87-97. DOI: 10.1016/j.coldregions.2017.11.012.*

Division on Engineering and Physical Sciences; Naval Studies Board; Committee on Autonomous Vehicles in Support of Naval Operations; National Academy of Sciences;. (2005). *Autonomous Vehicles in Support of Naval Operations.* National Academies Press.

DNV. (2010). *DNV-RP-C205 Environmental Conditions and Environmental Loads.* Oslo, Norway: Det Norske Veritas.

DNV-GL. (2018). *Rules for Classification, Naval Vessels, Part 4 Sub-surface ships, Chapter 1 Submarines.*

Domps, B., Dumas, D. G.-A., & Marmain, J. (2021). High-Frequency Radar Ocean Current Mapping at Rapid Scale With Autoregressive Modeling. *IEEE Journal of Oceanic Engineering.46:891-899. DOI: 10.1109/JOE.2020.3048507*.

Ellingsen, K., Ravndal, O., Reinås, L., Hansen, J., Marra, F., Myhre, E., . . . Sveberg, K. (2020). *RD 677082 - Subsea Shuttle Tanker System - Research Disclosure-Equinor.*

EPA. (2022, April). *Global Greenhouse Gas Emissions Data*. Retrieved from https://www.epa.gov/ghgemissions/global-greenhouse-gas-emissions-data

Equinor. (2019). Retrieved from https://www.equinor.com/news/archive/2019-03-14-extending-life-ncs

Equinor. (2021). *Energy Perspectives.* Equinor.

Equinor ASA. (2019). *Subsea shuttle system - Research Disclosure, vol. RD 662093.*

EY Global Power & Utilities. (2021). *Renewable Energy Country Attractiveness Index.* EY Global Power & Utilities.

Fortum. (2022). *A full-scale carbon capture and storage (CCS) project initiated in Norway*. Retrieved from https://www.fortum.com/media/2018/11/full-scale-carbon-capture-and-storage-ccs-project-initiated-norway

Fossen, T. (2011). *Handbook of Marine Craft Hydrodynamics and Motion Control.* West Sussex, UK: John Willey & Sons, Ltd.

Frank, D., Reichstein, M., Bahn, M., Thonicke, K., Frank, D., Mahecha, M., . . . Zscheischler, J. (2015). Effects of climate extremes on the terrestrial carbon cycle:concepts, processes and potential future impacts. *Global Change Biology (2015)21, 2861–2880, doi: 10.1111/gcb.12916.*

Gabler, U. (1972). *Submarine Construction, Technical Report.* Naval Ship Research and Development Centre.

Gaidai, O., Naess, A., Karpa, O., Xu, X., Cheng, Y., & Ye, R. (2019). Improving extreme wind speed prediction for North Sea offshore oil and gas fields. *Applied Ocean Research.88:63-70. DOI: 10.1016/j.apor.2019.04.024*.

Gaidai, O., Storhaug, G., & Naess, A. (2016). Extreme large cargo ship panel stresses by bivariate ACER method. *Ocean Engineering.123:432-439. DOI: 10.1016/j.oceaneng.2016.06.048*.

Global CCS Institute (1). (2021). *CCS in the circular carbon economy: policy & regulatory recommendations.*

Global CCS Institute (2). (2021). *Carbon capture and storage pipeline grows by 10 large-scale facilities globally.*

Global CCS Institute (3). (2021). *Storing carbon dioxide*. Retrieved from https://www.globalccsinstitute.com/about/what-is-ccs/storage/

Hamilton, T. M. (2014). *https://www.eia.gov/todayinenergy/detail.php?id=17991*. Retrieved from https://www.eia.gov.

Harms, A. A., Baetx, B. W., & Volti, R. R. (2005). *Engineering in time: the systematics of engineering history and its contemporary context.* Singapore: World Scientific Publishing Co. Pte. Ltd.

Huntington, H., Al-Fattah, S. M., Huang, Z., Gucwa, M., & Nouria, A. (2014). Oil Price Drivers and Movements: The Challenge for Future Research. *Alternative Investment Analyst Review*.

IEA. (2019). *The Role of CO2 Storage*. Retrieved from https://www.iea.org/reports/the-role-of-co2-storage

IEA. (2020). *The Role of CCUS in low-carbon power systems.* International Energy Agency (IEA).

IEA. (2022, March). *Global carbon dioxide emissions are set for their second-biggest increase in history*. Retrieved from https://www.iea.org/news/global-carbon-dioxide-emissions-are-set-for-their-second-biggest-increase-in-history

IMO. (2020, April). *Cutting sulphur oxide emissions*. Retrieved from https://www.imo.org/en/MediaCentre/HotTopics/Pages/Sulphur-2020.aspx

Journée, J., & Massie, W. (2001). *OFFSHORE HYDROMECHANICS (First Edition).* Delft University of Technology.

Karvonen, H., & Martio, J. (2018). SINTEF - Human Factors Issues In Maritime Autonomous Surface Ship Systems Development. *ICMASS*.

Kongsberg. (2019). *Marine Products and Systems.* Retrieved from https://www.kongsberg.com/globalassets/maritime/km-products/documents/product-catalog-2019.pdf

Kumar, A., & Jain, T. (2019). Linear Quadratic Optimal Control Design: A Novel Approach Based on Krotov Conditions. *Hindawi - Article ID 9490512, https://doi.org/10.1155/2019/9490512*.

Lee, J. D., & See, K. A. (2003). Trust in Automation: Designing for Appropriate Reliance. *SAGE Journals*.

Li, B. (2016). Dynamics and Control of Autonomous Underwater Vehicles With Internal Actuators. *Florida Atlantic University - Boca Raton, FL*.

Lichtblau, J. H. (1999). The Oil Price Collapse and Its Consequences At the Hearings “State of the Petroleum Industry". *U.S. Senate Committee on Energy & Natural Resources*.

Luenberger, D. (1972). *An introduction to observers.* IEEE Transactions on Automatic Control, 16(6), pp. 596-602.

Ma, Y., Da Silva, M. S., Xing, Y., & Sui, D. (2022a). Modelling of a Subsea Shuttle Tanker Hovering in Ocean Currents. *OMAE*.

Ma, Y., Xing, Y., Da Silva, M. S., & Sui, D. (2022b). Trajectory envelope of a subsea shuttle tanker hovering in stochastic ocean current. *Proceedings of the 41st International*

Conference of Ocean, Offshore and Arctic Engineering, 2022 June 5-10, Hamburg, Germany.

Ma, Y., Xing, Y., Ong, M. C., & Hemmingsen, T. H. (2021). Baseline design of a subsea shuttle tanker system for liquid carbon. *Ocean Engineering 240*.

Macrotrends. (2022, March). *Crude Oil Prices - 70 Year Historical Chart*. Retrieved from https://www.macrotrends.net/1369/crude-oil-price-history-chart

Maugeri, L. (2006). *The age of oil: the mythology, history and future of the world's most controversial resource.* Westport, Conn: Praeger.

Naess, A., & Gaidai, O. (2009). *Estimation of extreme values from sampled time series.* Structural Safety.31:325-334. DOI: 10.1016/j.strusafe.2008.06.021.

Naess, A., & Karpa, O. (2015). Statistics of extreme wind speeds and wave heights by the bivariate ACER method. *Mechanics and Arctic Engineering.137:021602. DOI: 10.1115/1.4029370*.

Naess, A., & Moan, T. (2013). *Stochastic dynamics of marine structures.* Cambridge: Cambridge University Press.

NFA. (2012). *Opportunities and Challenges for the Oil & Gas Industry.*

Northern Lights CCS. (2022). *What we do*. Retrieved from https://northernlightsccs.com/what-we-do/

NOAA. (2022, February). *Climate change: Global Temperature*. Retrieved from https://www.climate.gov/news-features/understanding-climate/climate-change-global-temperature

NSIDC(1). (2022, April). *April 2022 compared to previous years*. Retrieved from http://nsidc.org/arcticseaicenews/

NSIDC(2). (2022, April). *What are the impacts of Arctic sea ice loss?* Retrieved from https://nsidc.org/cryosphere/icelights/arctic-sea-ice-impacts

Odland, J. (2020). *OFF515 Offshore field development - Lecture notes.* University of Stavanger.

Our World in Data. (2022, March). *Global CO2 emissions from fossil fuels and land use change*. Retrieved from https://ourworldindata.org/co2-emissions

Papanikolaou, A. (2014). *Ship Design: Methodologies of Preliminary Design.* Dordrecht Heidelberg, New York, London: Springer.

Platts. (2022, March). *Platts periodic table of oil*. Retrieved from https://www.spglobal.com/commodityinsights/plattscontent/_assets/_files/downloads/crude_grades_periodic_table/crude_grades_periodic_table.html

Pugh, D. (1982). Estimating extreme currents by combining tidal and surge probabilities. *Ocean Engineering.9:361-372. DOI: 10.1016/0029-8018(82)90029-4*.

Renilson, M. (2018). *Submarine Hydrodynamics (second edition).* Springer International Publishing AG.

Ribeiro Mendes, C. H., Bentes, C. A., Rebelo, T. A., & Bousson, K. (2017). Guidance and Robust Control of a double-hull Autonomous Underwater Vehicle. *ICEUBI*.

Scheitrum, D. P., Carter, C. A., & Revoredo-Giha, C. (2018). WTI and Brent futures pricing structure. *Energy Economics 72 (2018) 462-469*.

SINTEF/The Norwegian CCS. (2020). *The Safety of CO2 storage*. Retrieved from https://blog.sintef.com/sintefenergy/ccs/the-safety-of-co2-storage/

Sorensen. (2018). *Marine Cybernetics (Lecture Notes).* Trondheim: Department of Marine Technology, NTNU.

Sorensen, B. (2011). *Renewable Energy: Physics, Engineering, Environmental Impacts, Economics and Planning.* San Diego: Elsevier Science & Technology.

Speight, J. G., Fantacci, L., & Speight, J. G. (2011). *An Introduction to Petroleum Technology, Economics, and Politics.* John Wiley & Sons, Incorporated.

The Maritime Industry Knowledge Center. (2022, April). *https://www.maritimeinfo.org/en/Blog/history-tankers-and-containerization*. Retrieved from https://www.maritimeinfo.org.

UNECA. (2021). *Harnessing renewable energy for industrialisation, economic diversification in Central Africa.* UNECA/ICE.

UNFCCC. (2022, April). *The Paris Agreement*. Retrieved from https://unfccc.int/process-and-meetings/the-paris-agreement/the-paris-agreement

Xing, Y., Gaidai, O., Ma, Y., Naess, A., & Wang, F. (2022). *A novel design approach for estimation of extreme responses of a subsea shuttle tanker hovering in ocean current considering aft thruster failure.* Applied Ocean Research 123 (2022) 103179.

Xing, Y., Ong, M., Hemmingsen, T., Ellingsen, K., & Reinås, L. (2021a). Design considerations of a subsea shuttle tanker system for liquid carbon dioxide transportation. *Journal of Offshore Mechanics and Arctic Engineering.143. DOI: 10.1115/1.4048926*.

Xing, Y., Santoso, T., & M. Y. (2021b). Technical–economic feasibility analysis of subsea shuttle tanker. *Journal of Marine Science and Engineering.10:20. DOI: 10.3390/jmse10010020*.

Xu, S., Ji, C.-y., & Soares, C. (2019). Estimation of short-term extreme responses of a semi-submersible moored. *Ocean Engineering.190:106388. DOI: 10.1016/j.oceaneng.2019.106388*.

Yu, S., Wu, W., Xie, B., Wang, S., & Naess, A. (2020). Extreme value prediction of current profiles in the South China Sea based on EOFs and the ACER method. *Applied Ocean Research.105:102408. DOI: 10.1016/j.apor.2020.102408*.

8 APPENDIX – PAPER DRAFT

International Conference on Ships and Offshore Structures
ICSOS 2022
17 – 19 October 2022, Ålesund, Norway

Station keeping of a subsea shuttle tanker system under extreme current during offloading

Yucong Ma[a,*], Terje Andreas Jevnaker[a], Yihan Xing[a]

[a]*University of Stavanger, Kjell Arholms gate 41,4021 Stavanger, Norway*

Abstract

A subsea shuttle tanker has been proposed as a multipurpose, versatile transport and storage system. This paper presents the station keeping challenge of the subsea shuttle tanker design during underwater loading and offloading at a subsea well under an extreme current environment. Understanding the behaviour of the proposed subsea shuttle tanker during offloading in extreme currents is vital for both the design of the subsea shuttle tanker itself but also the required actuator effort needed to uphold the demanded station-keeping abilities. During the offloading process, the hoovering subsea shuttle tanker would current-vane in a water depth of approximately 70 metres. Recent studies have shown that the drag force exerted on the subsea shuttle tanker body is up to 80 times larger for side-ways current compared to the head-on current. With current-vanning capabilities, the generated lift forces are low, and thus the subsea shuttle tanker will use less effort to maintain its desired position and water depth. The paper further investigates the movement of the subsea shuttle tanker during offloading with extreme current speeds, i.e., above 1.6 m/s, in the surge, heave and pitch motions, respectively. The planar model is built up using a Luenberger observer, where the vessel motions are measured and fed into a linear quadratic regulator (LQR) for calculations of the control input. The LQR control's primary focus is to hold and achieve the target for the subsea shuttle tanker during the offloading process, i.e., minimise the horizontal and vertical motion. Then, a state-of-the-art probabilistic method predicts the maximum and minimum potential depth excursion during offloading, i.e., the Average Exceedance Rate Method. This extreme value prediction result will serve as a basis for obtaining a cost-efficient design of the subsea shuttle tanker and provide recommendations for the decision-makers upon subsea shuttle tanker operation.

Keywords: Submarine; ACER method; Extreme response; LQR; Station keeping; Extra-large AUV

1. Introduction

1.1. Subsea shuttle tanker

Oil and gas production in the offshore environment has been evolving rapidly since the first offshore well was drilled in the Gulf of Mexico in 1947 (Bai and Bai 2018). Subsea pipelines and tanker ships have been utilised to transport the produced oil and gas from the offshore subsea fields to onshore facilities for refinement and delivery to the end consumer. However, technical and economic restrictions limit the applications of such transportation methods in some scenarios. The field development cost of submarine pipelines is directly proportional to the transportation distance and

* Corresponding author. *E-mail address: yucong.ma@uis.no*

inflates with the growth of water depth. Because of this, submarine pipelines are commonly installed for fields with large annuity close to the coast and are not feasible for remote fields with low profit margins. In this situation, tanker ships are deployed. Tanker ships are more flexible and can be easily switched to other fields depending on the demand. Still, these vessels are dependent on environmental circumstances and cannot work in severe sea states. Considering all these limitations, a subsea shuttle tanker (SST) system is proposed as a possible weather-independent transportation method for remote marginal fields.

The SST concept (as illustrated in Fig. 1) was first unveiled in two research disclosures by Equinor (Ellingsen et al. 2020, Equinor Energy AS 2019), in which multiple freight submersible concepts are proposed, such as train-like AUV, subsea glider, and SST. Xing et al. (2021a) focused on the SST concept and entailed the most critical design considerations of using civilian submersibles to transport liquid carbon dioxide. Based on these, a 34,000-tonne baseline design SST was presented by Ma et al. (2021). The baseline SST is an electric-propelled AUV with a liquid CO_2 capacity of 16,362 m^3, which can fulfil the annual need of any ongoing carbon capture and storage project in Norway.

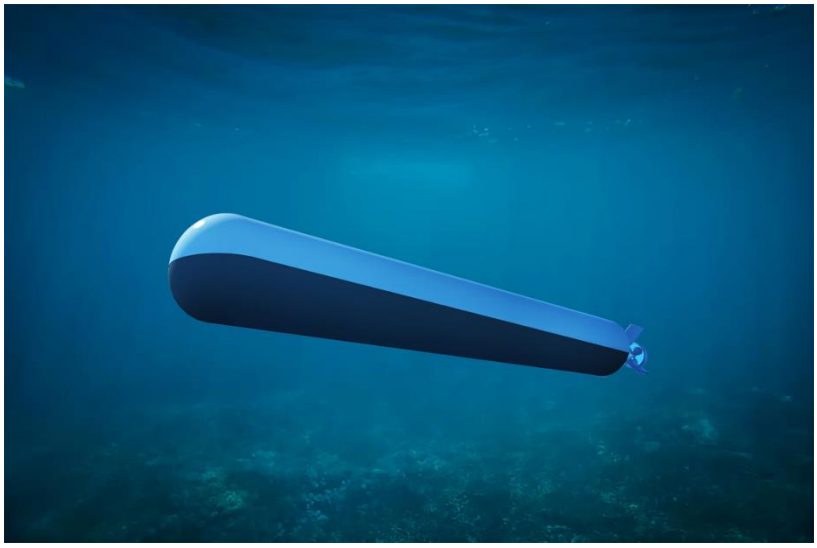

Fig. 1. Subsea shuttle tanker illustration.

The SST can help mitigate climate change and advance the industry towards net-zero as it is electrically propelled and therefore has zero carbon footprint during transportation. This contributes to the maritime industry's sustainability, with roughly 3.3% of the CO_2 emission resulting from fossil fuels (Papanikolaou 2014). In addition, a technical-economic study found that the SST can become the enabler to the utilisation of subsea fields with an annual storage capacity below 2.5 million tonnes per annual for carbon storage projects (Xing et al. 2021b).

1.2. Offloading process

The unloading process of the SST is illustrated in Fig. 2. The SST will first hover in vicinity above the subsea well during this process. Then, a remotely operated vehicle (ROV) deployed at the subsea well launches and carries a flowline to mate with the SST. After the flowline is appropriately connected, the SST discharges CO_2 to the wellhead. Meanwhile, it pumps in seawater to ensure neutral buoyancy. Finally, the ROV disconnects with the SST when this process is finished. The entire offloading operation consumes 4 hours. The SST is subjected to various environmental loads, as illustrated in Fig. 3, such as hydrostatic pressure, wave loads in shallow water, and ocean current.

Ocean current has the most considerable dynamic effects over the SST as it drives the vessel to an off-site away from its desired reference position. Therefore, the SST uses its hovering system consisting of a propeller and two thrusters to cope with the ocean current load. Smaller AUV designs often utilise vertical propellers or vertical ballast systems for accurate hovering control (Zhao et al. 2016). Though the ballast system can account for weight change during offloading, the thrusters will accommodate actuation at higher frequencies.

A comprehensive understanding of the motion in extreme currents is vital to the SST design. As a previous study shows, the side-way current drag is 80 times greater than the heading current, and the SST has to constantly head-on current while offloading (Ma et al. 2022). When the SST is facing ocean current, the surge off-site affects the required designed length of the flowline to avoid tautly and snap loads. The ocean current can also result in severe heave and pitch motions. This decides the maximum depth excursion of the SST, which determines the collapse pressure and is the dominating factor of the SST pressure hull design. The baseline SST applies the state-of-the-art engineering code (DNV 2018), which was commonly used on military submarines with heavy steel structures and closely arranged ring stiffeners. It suggested a high safety factor of 2.7 when determining the SST collapse pressure. However, as a merchant's vessel, it is essential for the SST to have an over 50% payload-over-displacement ratio to be economically feasible. Therefore, to reduce this safety factor, a throughout understanding of the nature of the SST manoeuvring is essential. In Ma and Xing (2022), the SST sailing operation is studied to identify the SST safety operational envelope (Burcher and Rydill 1994, Renilson 2018). The results suggest that with the current 19 bar (190 m depth) collapse pressure, the operational depth of the SST can be increased from 70 m to 110 m. Otherwise, the designed collapse pressure can be reduced correspondingly. This will potentially reduce structural weight and therefore increase the payload capacity. This work supports the design by looking into the extreme depth excursions during the other essential scenarios of the SST operation – offloading. The minimum depth excursion affects the safety depth of the SST during operation. It indicates the shallowest depth that the SST could ever reach during offloading. Knowing this is vital for the SST to avoid collision with large draught ships or other surface installations.

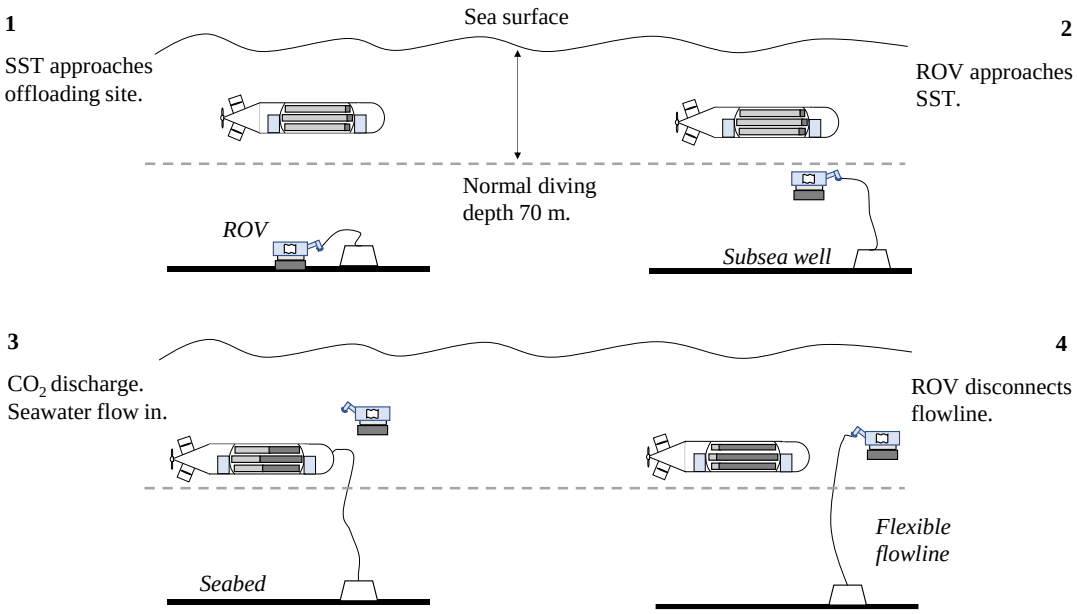

Fig. 2. Subsea shuttle tanker unloading sequence.

97

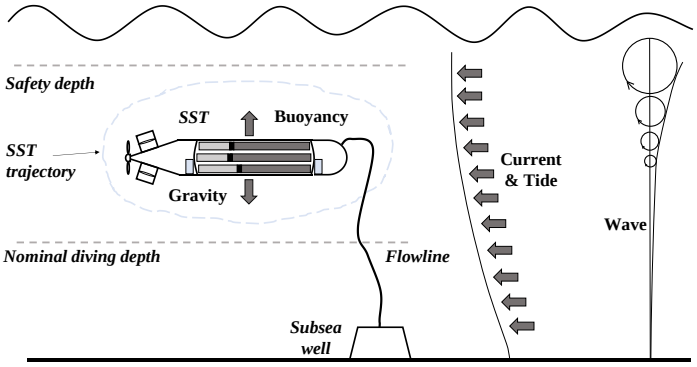

Fig. 3. Environmental loads that act on the SST during offloading.

98

99 Currently, the authors do not know that any research or studies within control theory and hovering
100 of AUVs with the proposed SST size in extreme current have been conducted. In an effort to close this
101 knowledge gap, the paper utilises the state-of-the-art ACER method to predict the maximum
102 displacement for the discretely sampled response process. Even though the control theory for
103 autonomous subsea vehicles is already widely explored, its application to the AUV of this class is still
104 left blank.

105 In this paper, the control and station keeping of the SST during the offloading process is studied
106 using a linear quadratic regulator (LQR). The main findings will be used as a basis to optimise the
107 baseline design cost-efficiently and provide suggestions for the operation of the SST. This process is
108 presented in Fig. 4. First, a non-linear planar manoeuvring model was proposed. After this, the SST
109 planar model is linearised to a simplified state-space model, which again is used to determine the
110 desired controller gain during offloading. Subsequently, a Luenberger observer measures the SST
111 motion response due to current and disturbance and feeds it back into the LQR control for calculations
112 of the control input. Ocean current is non-linear and changes with time and location. Modelling of the
113 ocean current follows a Gauss-Markov process, presented by Fossen (2021) and Sørensen (2018), also

employed by Ma et al. (2022) and Xing et al. (2022). A 50-year return period extreme currents above 1.6 m/s are introduced in this paper. Finally, the positional responses of the SST under extreme current are studied using the latest-developed averaged conditional exceedance rate (ACER) method.

This work adapted the hovering control system proposed and tuned by Ma et al. (2022). Later, the model was extended to investigate the SST depth excursion during aft thruster failure (Xing et al. 2022), which found that response at the SST aft, where thruster failure happens, has a 1.3-2.6 times larger response than the SST bow. This paper will focus on the integrated SST model but consider a 1.6 m/s extreme current speed and more considerable fluctuation. Twenty simulated 4-hour extreme values are used to predict the maximum response of the SST during hovering in extreme currents based on the ACER method. The ACER method, which was proposed in Naess and Gaidai (2009), is a Mote Carlo based state-of-the-art extreme value prediction method. It has been applied widely in engineering, especially naval architectures, to estimate structural responses (Gaidai et al. 2016, Xu et al. 2019) and sea states, such as wind (Gaidai et al. 2019), wave (Naess and Karpa 2015), and current profiles (Yu et al. 2020).

The paper structure is organised in the following manner: Section 2 introduces the SST planar model developed in Simulink. The control system is presented in Section 3. Then, Section 4 briefs the mathematics behind the ACER method. After that, the results are presented and discussed in Section 5. Finally, the main findings are summarised in Section 6.

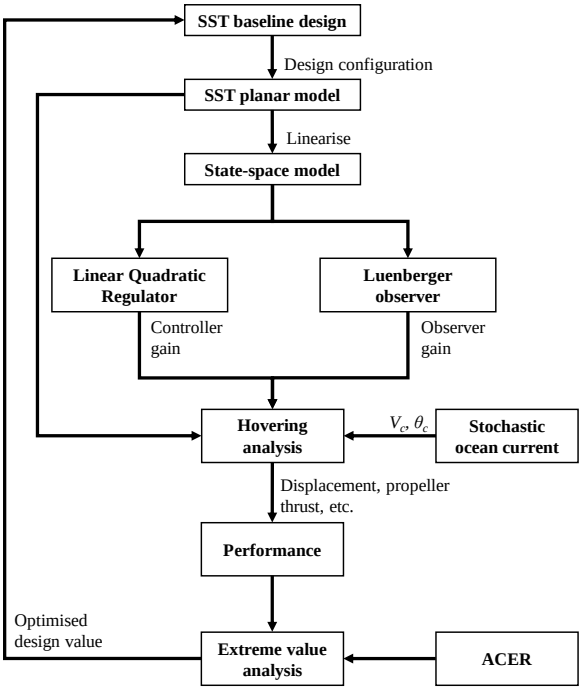

Fig. 4 Flowchart describing how hovering analysis under extreme stochastic current is done and how it serves for SST design.

2. SST planar model

2.1. Baseline SST design configurations

The most critical design parameters of the baseline SST (Ma et al. 2021) related to offloading modelling and analysis are summarised in Table 1. The coordinate system described in Section 2.2 is used in the table.

Table 1. Subsea shuttle tanker design parameters

Design configuration	Value	Design configuration	Value
Perpendicular length L_{pp} [m]	164	Bow, aft thruster thrust coefficient K_{Tt} [-]	0.4
Mid-body diameter D [m]	17	Propeller diameter d_p [m]	7
SST mass displacement Δ [tonnes]	33,600	Propeller thrust coefficient K_{Tp} [-]	0.19
Carbon dioxide capacity [m^3]	16,362	Safety depth [m]	40
Moment of inertia (pitch) I_{yy} [kg·m^2]	3.63×10^9	Nominal diving depth [m]	70
Centre of buoyancy [m]	[0, 0, -0.41]	Collapse diving depth [m]	190
Bow thruster location along SST length x_{tb} [m]	60	Designed collapse pressure [bar]	19
Aft thruster location along SST length x_{ta} [m]	-60	Structural design safety factor	2.7
Bow, aft thruster diameter d_t [m]	2		

The SST hovering system consists of its main propeller, two tunnel thrusters located at the bow and aft, and two compensation tanks situated at the bow and aft compartments for station keeping. The propeller and thrusters ensure that the SST maintains its position facing the current. The compensation tanks compensate for the mass difference sustained during offloading and guarantee the neutral buoyancy of the SST.

2.2. Coordinate system

The coordinate system setup of the SST is shown in Fig. 5. The body-fixed coordinate system is situated at the subsea shuttle tanker's centre of gravity (CoG). The origin of the SST body frame is relative to a global earth-fixed coordinate system based on the North-East-Down (NED) system. The centre of buoyancy, which is at the centroid of the subsea shuttle tanker, is located slightly above the CoG. In the figure, the positive global surge motion x points to the bow direction and, positive heave motion z points downward, positive pitch motion θ points from z-axis to x-axis; the velocities definition in the body frame are u, w, and q, respectively; the accelerations are $\dot{u}$, $\dot{w}$, and $\dot{q}$ correspondingly.

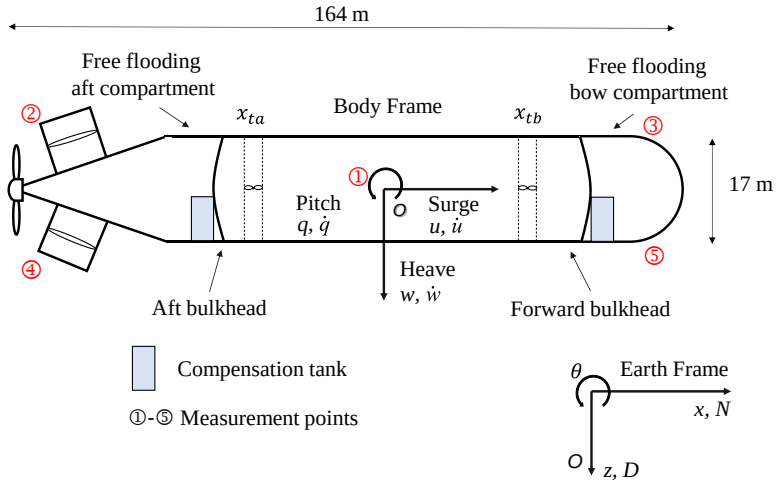

Fig. 5. SST body frame and earth frame coordinate system with measurement points.

2.3. Simulink model implementation

As presented in Fig. 6, the SST manoeuvring model is broken down into three categories:

- **SST plant model:** the SST plant model considers the hydrodynamic forces contributed by added mass, hydrodynamic drag, and body lift. The mathematic formulation of the plant model is explained in Section 2.4;
- **Actuator model:** the actuation system of the SST consists of the main propeller, tunnel thrusters, compensation (ballast) tanks, and aft hydroplanes. The main propeller, thrusters, and compensation tanks are used during offloading, and they are presented in Sections 2.5 and 2.6.
- **Ocean current model:** the current velocity and direction are modelled as stochastic processes. It is described in Section 2.7.

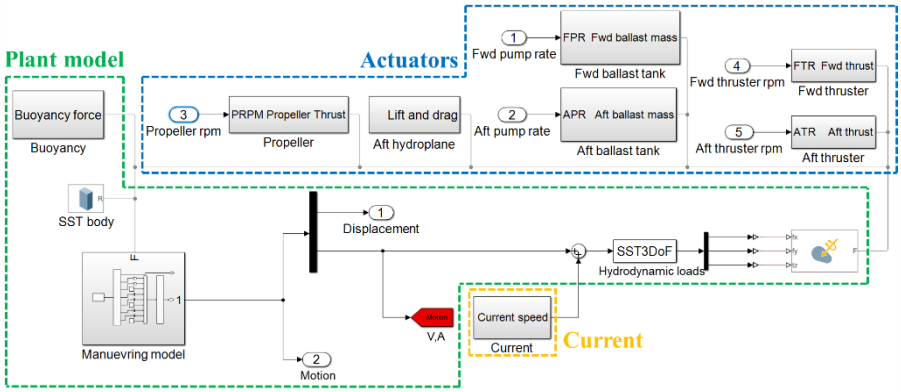

Fig. 6. Subsea shuttle tanker manoeuvring model in Simulink.

2.4. Vessel model

The equations of motion of the SST consist of kinetic equations of motion and dynamic equations of motion. Written in vectorial form, they are expressed as:

$$\begin{gathered} \dot{\boldsymbol{\eta}} = \boldsymbol{J}_{\boldsymbol{\Theta}}(\boldsymbol{\eta})\boldsymbol{\nu} \\ \boldsymbol{M}\dot{\boldsymbol{\nu}} + \boldsymbol{C}(\boldsymbol{\nu})\boldsymbol{\nu} + \boldsymbol{D}(\boldsymbol{\nu})\boldsymbol{\nu} + \boldsymbol{g}(\boldsymbol{\eta}) = \boldsymbol{\tau} \end{gathered} \tag{1}$$

In the equations, $\boldsymbol{\eta}$ is SST motion in global coordinate; $\boldsymbol{\nu}$ represents the velocity vector; $\boldsymbol{J}_{\boldsymbol{\Theta}}(\boldsymbol{\eta})$ is the matrix of Euler transformation; $\boldsymbol{M}$ is the matrix containing the mass and added mass of the SST; $\boldsymbol{C}(\boldsymbol{\nu})$ is a matrix containing the Coriolis-centripetal forces; $\boldsymbol{D}(\boldsymbol{\nu})$ is a matrix consisting of the hydrodynamic drag forces; $\boldsymbol{g}(\boldsymbol{\eta})$ is the vector for gravitational and hydrostatic forces; $\boldsymbol{\tau}$ is the control force vector.

The first equation can be expanded as:

$$\underbrace{\begin{bmatrix} \dot{N} \\ \dot{D} \\ \dot{\theta} \end{bmatrix}}_{\dot{\boldsymbol{\eta}}} = \underbrace{\begin{bmatrix} \cos\theta & \sin\theta & 0 \\ -\sin\theta & \cos\theta & 0 \\ 0 & 0 & 1 \end{bmatrix}}_{\boldsymbol{J}_{\boldsymbol{\Theta}}(\boldsymbol{\eta})} \underbrace{\begin{bmatrix} u \\ w \\ q \end{bmatrix}}_{\boldsymbol{\nu}} \tag{2}$$

where the notations of the motions are illustrated in Fig. 5.

The matrices in the dynamic equations of motion (1) can be expanded as (3)-(5):

$$\boldsymbol{M} = \begin{bmatrix} m - X_{\dot{u}} & 0 & mz_g \\ 0 & m - Z_{\dot{w}} & -Z_{\dot{q}} \\ mz_g & M_{\dot{w}} & I_{yy} - M_{\dot{q}} \end{bmatrix} \tag{3}$$

$$\boldsymbol{C}(\boldsymbol{v}) = \begin{bmatrix} 0 & 0 & 0 \\ 0 & m - Z_{\dot{w}} & -(m - X_{\dot{u}})u \\ 0 & (Z_{\dot{w}} - X_{\dot{u}}) & 0 \end{bmatrix} \tag{4}$$

$$\boldsymbol{D}(\boldsymbol{v}) = \begin{bmatrix} X_{|u|u}|u| & X_{wq}q & X_{qq}q \\ Z_{uq}q & Z_{|w|w} + Z_{uw}u & Z_{q|q|} \\ M_{uw}w & M_{|w|w} & M_{uq}u + M_{|q|q} \end{bmatrix} \tag{5}$$

where $X_{\dot{u}}$, $Z_{\dot{w}}$, $Z_{\dot{q}}$, $M_{\dot{w}}$, and $M_{\dot{q}}$ are added mass hydrodynamic coefficients; $X_{|u|u}$, $Z_{|w|w}$, $Z_{|q|q}$, $M_{|w|w}$, and $M_{|q|q}$ are drag terms; X_{wq}, X_{qq}, Z_{uw}, Z_{uq}, and M_{uq} are cross-term added mass hydrodynamic coefficients; Z_{uw} is the body lift and M_{uw} is the Munk moment. The hydrodynamic derivatives used in this study are listed in Table 2.

Table 2. Hydrodynamic derivatives.

Parameter	Value	Unit	Parameter	Value	Unit
$X_{\dot{u}}$	-5.14×10^5	kg	$Z_{|q|q}$	4.79×10^9	kg·m
$Z_{\dot{w}}$	-3.29×10^7	kg	$M_{|q|q}$	-4.34×10^{12}	kg·m^2
$M_{\dot{w}}$	-4.40×10^8	kg·m	X_{wq}	-3.28×10^7	kg
$Z_{\dot{q}}$	-4.40×10^8	kg·m	X_{qq}	-4.40×10^8	kg·m
$M_{\dot{q}}$	-6.39×10^{10}	kg·m^2	Z_{uq}	5.14×10^5	kg
$X_{|u|u}$	-1.64×10^4	kg/m	M_{uq}	-4.40×10^8	kg·m
$Z_{|w|w}$	-1.42×10^6	kg/m	Z_{uw}	-2.42×10^5	kg/m
$M_{|w|w}$	1.67×10^7	kg	M_{uw}	-3.99×10^7	kg

2.5. Propeller model

The SST propeller design is provided by Ma et al. (2021), in which a Wageningen B3-30 propeller is selected. It is 3-bladed and has a small aspect ratio of 0.30. The diameter of the propeller d_p is 7 m. During the 4-hour unloading simulation process, the mean current velocity is constant. Consequently, a constant thrust coefficient $K_{Tp} = 0.17$ is used. Therefore, the thrust of the main propeller can be obtained as:

$$F_P = K_{Tp} \cdot \rho \cdot n_p \cdot |n_p| \cdot d_p^4 \tag{6}$$

where ρ is seawater density and n_p is propeller rotational speed.

188 *2.6. Tunnel thruster model*

189 Two identical tunnel thrusters are equipped on the SST for hovering control (Ma et al. 2022, Xing et
190 al. 2022). Their positions are illustrated in Fig. 5 and the configurations are listed in Table 1. The
191 thrusters' forces result in heave forces and pitching moments on the SST. The contribution from
192 individual thruster can be expressed as:

$$F_T = K_{Tt} \cdot \rho \cdot n_t \cdot |n_t| \cdot d_t^4 \tag{7}$$

193 where F_T is the thruster thrust and n_t is the thruster revolution speed. As the advanced speed for
194 tunnel thrusters is minimal, the advanced number is approximately 0. Consequently, the thruster thrust
195 coefficient is a constant of 0.4.
196 The thruster vector $\boldsymbol{\tau_T}$ consisting of the propeller and thrusters' contributions in the surge, heave,
197 and pitch can be summarised as:

$$\boldsymbol{\tau_T} = \begin{bmatrix} F_P \\ F_{Tb} + F_{Ta} \\ F_{Tb}x_{Tb} + F_{Ta}x_{Ta} \end{bmatrix} \tag{8}$$

198 where F_{Tb} and F_{Ta}, as calculated by (7), are thrusts from the bow and aft thrusters, respectively.

199 *2.7. Stochastic current model*

200 Numerous research and guidelines have introduced the modelling of stationary current (DNV 2010,
201 Domps et al. 2021, Yu et al. 2020). However, these models are not sufficient to study the positioning
202 problem of the SST subjected to time-varying current. Therefore, a stochastic current model presented
203 by Fossen (2021) and Sørensen (2018) is adapted to this study to consider current velocity variation.
204 The current is represented by two variants: current velocity V_c and current inflow angle θ_c. They both
205 follow the first-order Gauss-Markov process:

$$\dot{V}_c + \mu_1 V_c = \omega_1 \tag{9}$$

$$\dot{\theta}_c + \mu_2 \theta_c = \omega_2 \tag{10}$$

206 where μ_1 and μ_2 are time constants with nonnegative values, according to Fossen (2021). ω_1 and
207 ω_2 are Gaussian white noise. To exemplify, the time constants are set to be 1 in this work. The noise
208 power of the Gaussian white noise is set to 0.1 when rendering the turbulency of the inflow.
209 For 2D irrotational current, the current velocity in the global frame can be expressed as:

$$\boldsymbol{v_c^g} = \begin{bmatrix} V_c \cos\theta_c \\ V_c \sin\theta_c \\ 0 \end{bmatrix} \tag{11}$$

210 Therefore, the current velocity described in the SST body frame can be expressed as:

$$\boldsymbol{v}_c^b = \begin{bmatrix} V_c \cos(\theta_c - \theta) \\ -V_c \sin(\theta_c - \theta) \\ 0 \end{bmatrix} \tag{12}$$

Finally, the relative velocity is obtained by summing up $\boldsymbol{v}_c^b$ and $\dot{\boldsymbol{\eta}}$.

Current data in the North Sea is used as the baseline SST designed to be deployed in the Norwegian sector. Extreme current velocity is determined based on the work conducted in Pugh (1982), which estimated the extreme current distributions and velocities by applying joint tide-surge probability techniques to the observation data in Inner Dowsing, North Sea. The extreme current prediction result is summarised in Fig. 7. The figure shows that the maximum current velocity is observed at the South-West 165 ° direction, where the corresponding extreme current speed is 1.6 m/s with a 50-year return period.

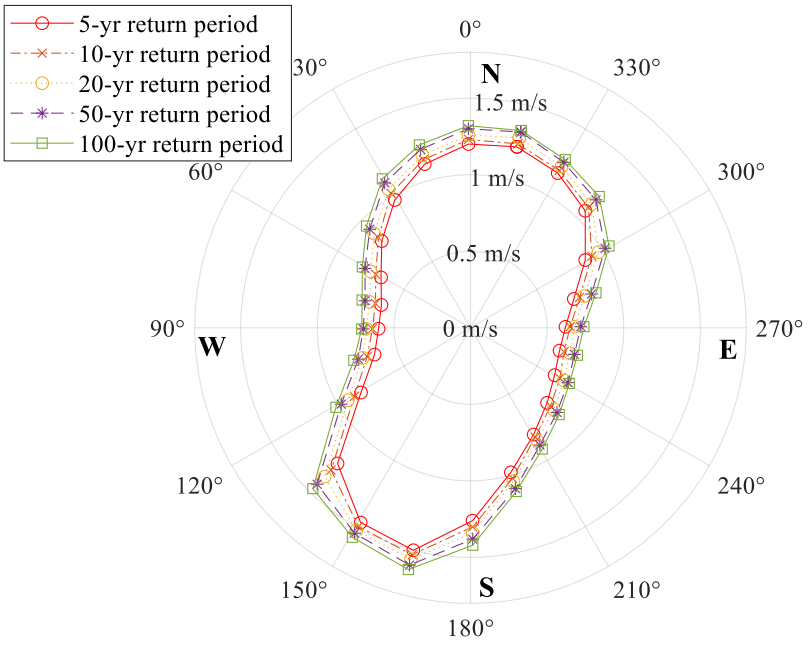

Fig. 7. Extreme current velocity distribution at Inner Dowsing (data from Pugh (1982)).

3. Control system design

The control system used for the SST hovering, an LQR, was initially designed by Ma et al. (2022) and then extended by Xing et al. (2022). The control diagram is presented in Fig. 8. An LQR is a full-state feedback optimal control method which aims to solve the optimisation problem at hand, i.e., performance versus effort, and thereby find the state feedback controller gain $\boldsymbol{K}$. Defining the performance and effort parameters will be influenced by the desired properties of the subsea shuttle tanker. E.g., one specific gain matrix can be determined by imposing importance on the stability of the subsea shuttle tanker under the offloading process (i.e., a minimal movement is required). This would increase actuator efforts and consequently reduce the energy storage and subsea shuttle tanker range at a higher rate.

On the other hand, if the design of the subsea shuttle tanker would present more flexibility in the movement during offloading, we would penalise actuator effort to reduce the energy consumption during the offloading process. This would then give us a different gain matrix $\boldsymbol{K}$.

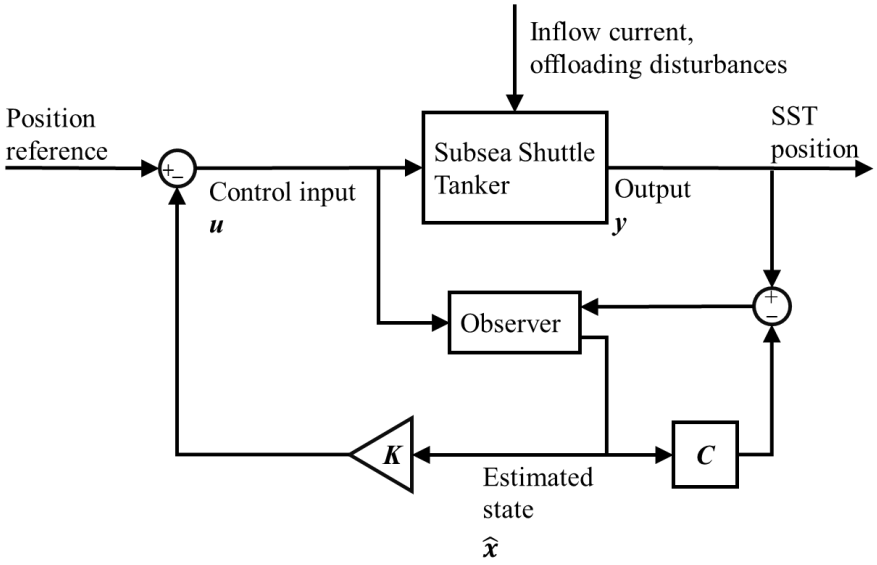

Fig. 8. SST control block diagram.

3.1. Linear state-space model

3.1.1. Linear state-space function

The SST model is highly coupled, non-linear, and time-variant. In the design of an LQR, a linear time-invariant state-space model is obtained using a MATLAB model linearizer. The linear state-space equations for the subsea shuttle tanker are presented in (13) and (14):

$$\dot{\boldsymbol{x}} = \boldsymbol{A}\boldsymbol{x} + \boldsymbol{B}\boldsymbol{u} \tag{13}$$

$$\boldsymbol{y} = \boldsymbol{C}\boldsymbol{x} \tag{14}$$

where $\boldsymbol{x}$ represents the state of the system (state vector), and $\boldsymbol{y}$ represents the output of the system (output vector). The vector $\boldsymbol{u}$ is called the control vector and represents the control input. Matrix $\boldsymbol{A}$, $\boldsymbol{B}$ and $\boldsymbol{C}$ are state, input, and output matrices, respectively.

3.1.2. Model linearisation

The subsea shuttle tanker manoeuvring is dynamic, non-linear, and coupled by nature. By linearising the model, we can attain the linear space-state function.

- Input of linearised model, $\boldsymbol{u} = [\boldsymbol{n_{tb}}; \boldsymbol{n_p}; \boldsymbol{n_{ta}}]$;
- Output of linearised model, $\boldsymbol{y} = [\boldsymbol{N}; \boldsymbol{D}; \boldsymbol{\theta}]$;
- Obtained state vector, $\boldsymbol{x} = [\boldsymbol{N}; \boldsymbol{D}; \boldsymbol{\theta}; \dot{\boldsymbol{N}}; \dot{\boldsymbol{D}}; \dot{\boldsymbol{\theta}}]$.

The linearisation approximation of the non-linear system will only be valid in a small region around the chosen operating point. The relevant operating point for the linearisation of the manoeuvring model is specified as a 1 m/s design current speed with an inflow angle of 1 °. $\boldsymbol{A}$, $\boldsymbol{B}$ and $\boldsymbol{C}$ are a 6 × 6, 6 × 3, and 3 × 6 matrices, respectively. The linearised state-space model is obtained as follows:

$$\boldsymbol{A} = \begin{bmatrix} 0 & 0 & 0 & 1 & 0 & 0 \\ 0 & 0 & 0 & 0 & 1 & 0 \\ 0 & 0 & 0 & 0 & 0 & 1 \\ 0 & 0 & 2.65 \times 10^{-5} & -1.00 \times 10^{-3} & -1.21 \times 10^{-4} & -1.45 \times 10^{-2} \\ 0 & 0 & 2.87 \times 10^{-6} & -1.32 \times 10^{-4} & -8.91 \times 10^{-3} & 5.18 \times 10^{-2} \\ 0 & 0 & -2.37 \times 10^{-2} & 6.21 \times 10^{-5} & 3.87 \times 10^{-3} & -5.96 \times 10^{-2} \end{bmatrix} \tag{15}$$

$$\boldsymbol{B} = \begin{bmatrix} 0 & 0 & 0 \\ 0 & 0 & 0 \\ 0 & 0 & 0 \\ 2.54 \times 10^{-10} & -8.80 \times 10^{-5} & 4.24 \times 10^{-10} \\ 3.84 \times 10^{-6} & -5.25 \times 10^{-9} & 6.40 \times 10^{-6} \\ 7.13 \times 10^{-7} & 0 & -1.19 \times 10^{-6} \end{bmatrix} \tag{16}$$

$$\boldsymbol{C} = \begin{bmatrix} 1 & 0 & 0 & 0 & 0 & 0 \\ 0 & 1 & 0 & 0 & 0 & 0 \\ 0 & 0 & 1 & 0 & 0 & 0 \end{bmatrix} \tag{17}$$

3.2. Linear Quadratic Regulator

As the LQR is an optimal control, it aims to solve the optimisation problem, i.e., performance versus effort, and thereby find the gain matrix $\boldsymbol{K}$. For the time-invariant system expressed in (13) and (14), the LQR solves the quadratic weighted cost functions and approaches the optimal gain based on our weighted performance and effort (Fossen 2021).

Equation (29) shows the minimised quadratic cost function, where $\boldsymbol{Q}$ represents the performance and $\boldsymbol{R}$ represents the effort.

$$\boldsymbol{L}(\boldsymbol{x}, \boldsymbol{u}) = \int_0^\infty (\boldsymbol{x}^T \boldsymbol{Q} \boldsymbol{x} + \boldsymbol{u}^T \boldsymbol{R} \boldsymbol{u}) dt \tag{18}$$

The state weighting matrix is defined as $\boldsymbol{Q} = \boldsymbol{Q}^{\boldsymbol{T}} \geq \boldsymbol{0}$, and the energy weighting matrix for the actuator is defined as $\boldsymbol{R} = \boldsymbol{R}^{\boldsymbol{T}} \geq \boldsymbol{0}$. These weighting matrices give us the importance of the state error together with the power consumption of the actuator system.

By differentiating between the initial state of the system and the desired state of the system, we can penalise the different states and efforts, i.e., adjusting the diagonal elements in the matrix $\boldsymbol{Q}$ and $\boldsymbol{R}$, respectively. By doing this, the most optimal solution based on our relative weights of the performance and effort is obtained.

The control law for LQR is obtained by solving the LQR problem and is described as:

$$\boldsymbol{u} = -\boldsymbol{K}\boldsymbol{x} \tag{19}$$

where the gain matrix $\boldsymbol{K}$ is a 3×6 matrix derived from an optimisation problem.

When designing a linear quadratic regulator, the controllability of the subsea shuttle tanker must be satisfied. The linear state matrix $\boldsymbol{A}$ and linear input matrix $\boldsymbol{B}$ must be controllable for the planar

model. The controllability matrix $\boldsymbol{Con}$ must have full rank (i.e., its rank, number of linearly independent rows equals the largest possible for the matrices of the same dimensions) and must thus have a right inverse.

$$\boldsymbol{Con} = [\boldsymbol{B}|\boldsymbol{AB}|\cdots|\boldsymbol{A^{n-1}B}] \tag{20}$$

The controllability matrix for the subsea shuttle tanker linearised model displays a controllability matrix of 6, i.e., the system is controllable.

3.3. State observer

As Fig. 8 displays, a Luenberger observer (state observer or state estimator) (Luenberger 1971) is included in the block design for monitoring the system states. By representing sensors, the Luenberger observer is a system that estimates the internal state of the subsea shuttle tanker. Understanding the internal states of the physical subsea shuttle tanker system during offloading is critical for the design of the motion controller. The estimated state $\hat{\boldsymbol{x}}$ is based on the control input $\boldsymbol{u}$ and the system output $\boldsymbol{y}$. The system is assumed to be observable, and the system's state can thus be constructed by $\boldsymbol{u}$ and $\boldsymbol{y}$ in a finite time interval.

The observer is mathematically modelled as per (21).

$$\dot{\hat{\boldsymbol{x}}} = \boldsymbol{Ax} + \boldsymbol{Bu} + \boldsymbol{K_L}(\boldsymbol{y} - \hat{\boldsymbol{y}}) \tag{21}$$

where $\boldsymbol{K_L}$ represents the observer gain and $\hat{\boldsymbol{y}}$ is an estimation of the output vector $\boldsymbol{y}$. Ma et al. (2022) performed the observer gain sensitivity analysis, which shows that the observer performance increases with moving the pole position further to the negative axis. Identical to Ma et al. (2022), the pole position of $\boldsymbol{p} = [-4; -4; -2; -2; -2]$ is used in this work.

Similarly, the system needs to be observable before implementing the Luenberger observer; the observability matrix $\boldsymbol{Obs}$ (22) of the SST has a full column 6.

$$\boldsymbol{Obs} = [\boldsymbol{C}^\top|\boldsymbol{A}^\top\boldsymbol{C}^\top|\cdots|(\boldsymbol{A}^\top)^{n-1}\boldsymbol{C}^\top] \tag{22}$$

4. Average conditional exceedance rate method

The average conditional exceedance rate (ACER) is used in extreme value predictions and distributions, and the method was introduced by Naess and Gaidai (2009). This extreme value prediction is made by constructing a series of non-parametric functions not based on asymptotic sample theory. The method has been applied for stationary and non-stationary stochastic processes and includes all global maximum peaks. It also avoids the necessity of declustering of data to ensure independence (Karpa 2015). From Xing et al. (2022), it was manifested that the extreme responses were twice as high for a 5-year return period compared to the maxima of a 4-hour response period.

For response processes of marine structures, the Gumbel distribution would almost always be the appropriate one (Naess and Moan 2013). Compared to other extreme value estimation techniques such as generalised extreme value distribution and peaks-over-threshold method, ACER does not require the observations to be independent and identical distributed, i.e., each random variable will have the same probability distribution as the other random variables. No outcome will influence other outcomes (independent), and all samples come from the same distribution (identical). The non-parametric

functions based on ACER functions of various orders are developed, and the aim of these is to approximate the actual extreme value distribution.

In detail, the ACER method determines the distribution function of the extreme value, which is denoted $M_N = max\{X_j;\ j = 1,\ \cdots,\ N\}$. An accurate estimation of $P_\eta = Prob(M_N \leq \eta)$ is wanted for large values of η. It denotes the probability of the occurrence of the extreme value η and it follows:

$$P_\eta = Prob(M_N \leq \eta) = Prob(X_1 \leq \eta,\ \cdots,\ X_N \leq \eta) \tag{23}$$

Solving this equation, a succession of conditional approximation $P_k(\eta)$ is used, where $P_k(\eta)$ tends to be close to P_η as k increases. For $N \gg 1$ and $k = 1,2,\cdots$, $P_k(\eta)$ is represented as (Naess and Gaidai 2009):

$$P_k(\eta) \approx exp(-\sum_{j=k}^{N} \alpha_{kj}(\eta)) \tag{24}$$

where $\alpha_{kj}(\eta) = Prob\big(X_1 > \eta | X_{j-1} \ll \eta,\ \cdots,\ X_{j-k+1} \leq \eta\big)$ and it represents the exceedance probability (only counted if proceeded by non-exceedances). The notion described in (24) and will be calculated by ACER as follows:

$$\varepsilon_k(\eta) = \frac{1}{N-k+1}\sum_{j=k}^{N} \alpha_{kj}(\eta)\,, k = 1,2,\cdots \tag{25}$$

where N represents the number of sample points for a specific moment X_n. Onwards, for $k \geq 2$, $\tilde{\varepsilon}_k(\eta)$ is used instead of $\varepsilon_k(\eta)$. This is done because it is easier to use for non-stationary or long-term statistics (Naess and Moan 2013), and it is defined as:

$$\tilde{\varepsilon}_k(\eta) = \lim_{N\to\infty} \frac{\sum_{j=k}^{N} a_{kj}(\eta)}{N-k+1} \tag{26}$$

$$\lim_{N\to\infty} \frac{\tilde{\varepsilon}_k(\eta)}{\varepsilon_k(\eta)} = 1. \tag{27}$$

where $a_{kj}(\eta)$ is the realised values for the observed time series, and (27) needs to be fulfilled. The ACER (for both stationary and non-stationary time series) sample estimate can be denoted as:

$$\hat{\varepsilon}_k(\eta) = \frac{1}{R}\sum_{r=1}^{R} \hat{\varepsilon}_k{}^{(r)}(\eta) \tag{28}$$

where R is the number of samples or realisations, and

$$\hat{\varepsilon}_k{}^{(r)}(\eta) = \frac{\sum_{j=k}^{N} a_{kj}{}^{(r)}(\eta)}{N-k+1} \tag{29}$$

where r denotes the specific realisation number.

With sufficient numbers of realisations and assumed independent, the 95% confidence interval (CI) for the $\varepsilon_k(\eta)$ can be estimated as:

$$CI(\eta) = \hat{\varepsilon}_k(\eta) \pm \frac{1.96\hat{s}_k(\eta)}{\sqrt{R}} \tag{30}$$

where $\hat{s}_k(\eta)$ refers to the sample standard deviation of samples and can be estimated by:

$$\hat{s}_k(\eta)^{\,2} = \frac{1}{R-1}\sum_{r=1}^{R}(\hat{\varepsilon}_k{}^{(r)}(\eta) - \hat{\varepsilon}_k(\eta))^2 \tag{31}$$

The above equations for estimation of average exceedance rate are based on direct numerical simulations. In contrast, an extrapolation technique can reduce the computational time. Assuming the mean exceedance rate in the tail behaves similarly to $exp\{-a(\eta-b)^c\}\,(\eta \geq \eta_0 \geq b)$ where a, b and c are suitable constants. The ACER will therefore be assumed by:

$$\varepsilon_k(\eta) \approx q_k(\eta) exp\{-a_k(\eta - b_k)^{c_k}\} \tag{32}$$

where $\eta \geq \eta_1 \geq b_k$ and the function $q_k(\eta)$ varies slowly compared to the exponential function $exp\{-a_k(\eta-b_k)^{c_k}\}$ in the tail region. Continuously, this can be replaced by a constant for a fitting choice of the tail marker η_0. In the end, the Levenberg-Marquardt least-squares optimisation method can be used to determine the constants $a_k, b_k, c_k \; and \; q_k$. Naess and Gaidai (2009) expressed their experience that this damped least-squares method is well suited for this assignment. Chai et al. (2018) concluded that the extrapolation scheme applied to capture the tail behaviour of the ACER functions was satisfactory for the extreme value predictions.

5. Results and discussion

5.1. Time-domain response

In total, an 80-hour realisation consisting of 20 independent 4-hour simulations is performed in Simulink. Fig. 9 exemplifies a 500 s stochastic current realisation. The mean current velocity is set to be 1.6 m/s while the mean inflow angle is 0 °. Correspondingly, Fig. 10 exemplifies the response of the SST, i.e., SST state vector $\boldsymbol{x} = [\boldsymbol{N}; \boldsymbol{D}; \boldsymbol{\theta}; \dot{\boldsymbol{N}}; \dot{\boldsymbol{D}}; \dot{\boldsymbol{\theta}}]$, in the global coordinate system to present the performance of the controller and the observer. Both measured states and actual states are given. As shown in Fig. 10 (a), the observer can provide excellent measurement for the SST surge, heave, and pitch displacement, as shown in Fig. 10 (b), the observed values for surge, heave, and pitch velocities are close to the actual velocities of the SST. In the presented time series, the SST has a steady surge off-site of approximately 1.2 m with a fluctuation amplitude of about 0.2 m. On the contrary, the heave

motion of the SST has an amplitude of around 2 metres, significantly more significant than the surge displacement. This is caused by the giant side-way drag force. The pitch motion of the SST in the presented case is lower than 0.04 rad. As the SST has a length of 164 m, this can still result in an over 2 metres off-site to the bow and aft.

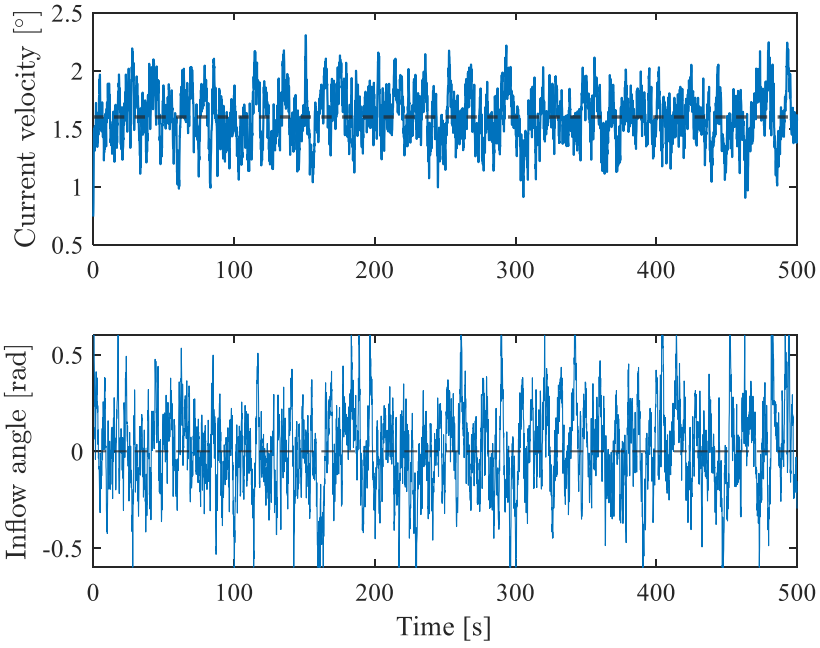

Fig. 9 Exemplified current realisation.

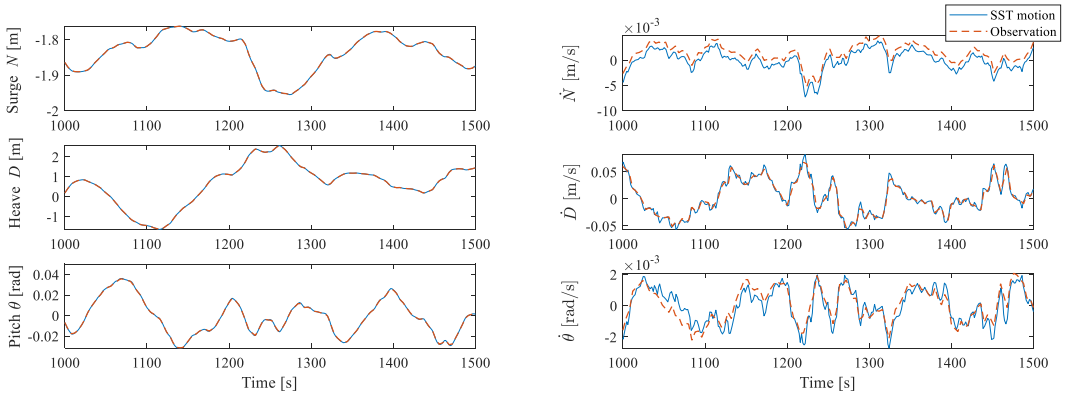

(a) (b)

Fig. 10 SST response in 500 s realisation. (a) SST motion. (b) SST velocity.

From the SST time series, the responses of the five measurement points (ref. Fig. 5) are obtained. The maximum and minimum depth excursions in the 20 realisations for the five points are presented in Fig. 11 (a) and Fig. 11 (b). These are the inherent values to study the depth excursions of the SST and further predict the long-term extreme depth off-site of the SST, which helps determine the values bringing a cost-efficient design. Essentially, the extreme depth excursions happen at the vessel's bow and aft, rather than the positions close to the mid-vessel, as the motions at those positions have contributed from the pitch motion. Therefore, the minimum depth excursions are expected at the bow

and aft of the upper bound of the SST, i.e., Point 3 and Point 2, as shown in Fig. 11 (b). While the maximum depth is reached by the bow and aft of the lower bound, i.e., Point 4 and Point 5, measurement point 1 locates at the centroid of the SST and is provided as a reference.

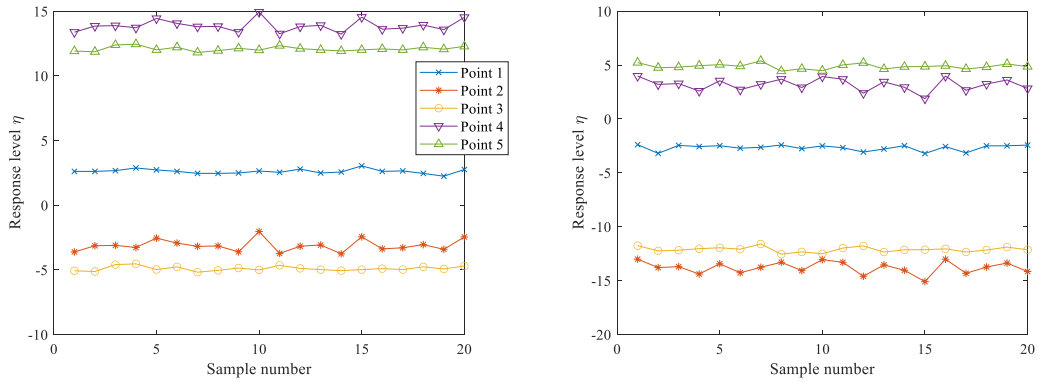

(a) (b)

Fig. 11 Peak value in each realisation. Point 1 to 5 are illustrated in Fig. 5. (a) Maximum depth excursion. (b) Minimum depth excursion.

5.2. k value selection

As mentioned in Section 4 and Naess and Gaidai (2009), the cascade of conditioning approximations $P_k(\eta)$ converge toward $P(\eta)$ when k increases. k value from 1-6 is checked in this study. The result for Point 4 maximum depth excursion is presented, for instance, in Fig. 12. It can be noticed that for k from 1 to 6; the response η is at the same level. However, with the same $ACER_k(\eta)$, η is more conservative (larger) for $k = 1$ while the values for $k \geq 2$ are very close. Therefore, it is concluded that applying $k = 2$ returns an accurate prediction of the SST extreme depth excursion for the measured points.

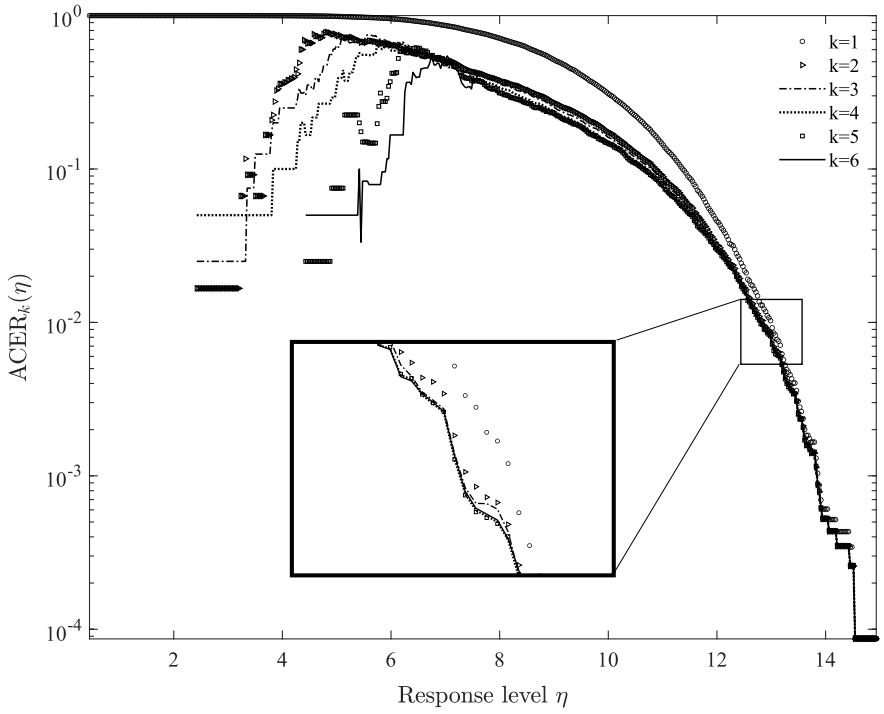

Fig. 12 ACER functions for maximum depth excursion of Point 4 with different k values.

5.3. Extreme depth excursion predicted by ACER method

The extreme depth excursions of the SST measurement points using the ACER method for the 80-hour simulations are discussed in this section. Fig. 13 and Fig. 14 present the extrapolation results with an exceedance rate of 1×10^{-6} of the minimum and maximum depth excursion, respectively. The 95 % confidence interval (CI) is presented in a dashed line, and the fitted 95 % CI is presented in dotted lines. A close fit to the simulation results can be observed for the ACER method.

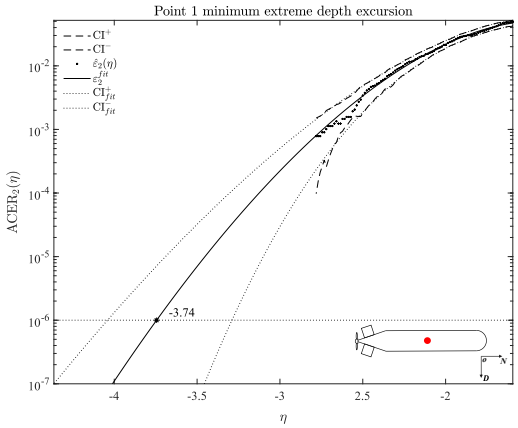

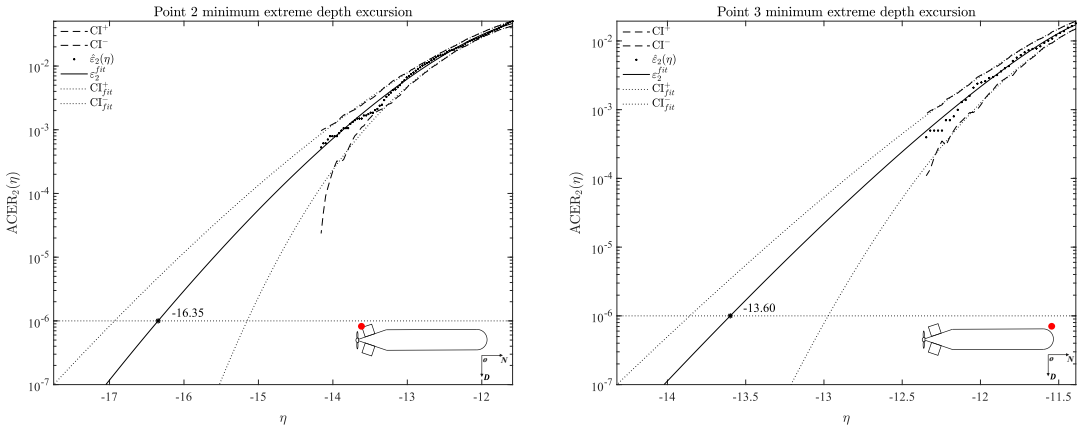

Fig. 13 ACER extrapolation for minimum depth excursion. (a) Point 1. (b) Point 2. (c) Point 3.

The minimum extreme response of the SST is observed at Point 2, as shown in Fig. 13 (b)). The value with a 1×10^{-6} exceedance rate is -16.35 m from the reference offloading position, 2.75 m above the value for the SST bow. As a reference, this extreme value for the SST centroid (Point 1) is -3.74 m. The results indicate that if the SST offloads at 40 m safety depth, the minimum extreme depth excursion is 23.65 m (upper bound).

The maximum positive off-site (lower bound) is also observed at the aft (Point 4). Its value is 15.98 m, slightly lower than the absolute minimum depth excursion (16.35 m). The maximum extreme depth at the SST bow (Point 5) is 2.32 m smaller. The maximum extreme off-site for Point 1 is 3.74 m, the same as the absolute minimum extreme. Therefore, when the SST is offloading at a 70 m water depth, the maximum depth excursion of the SST with a 1×10^{-6} exceedance rate is 86 m.

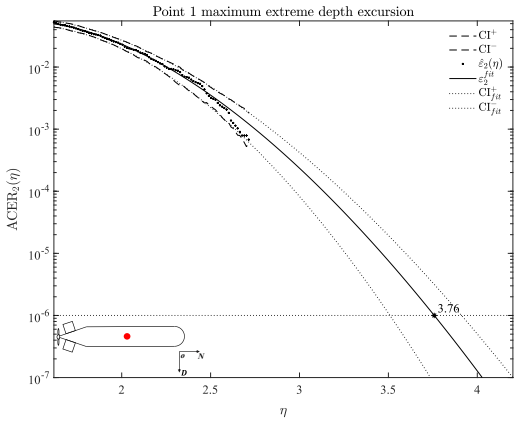

(a)

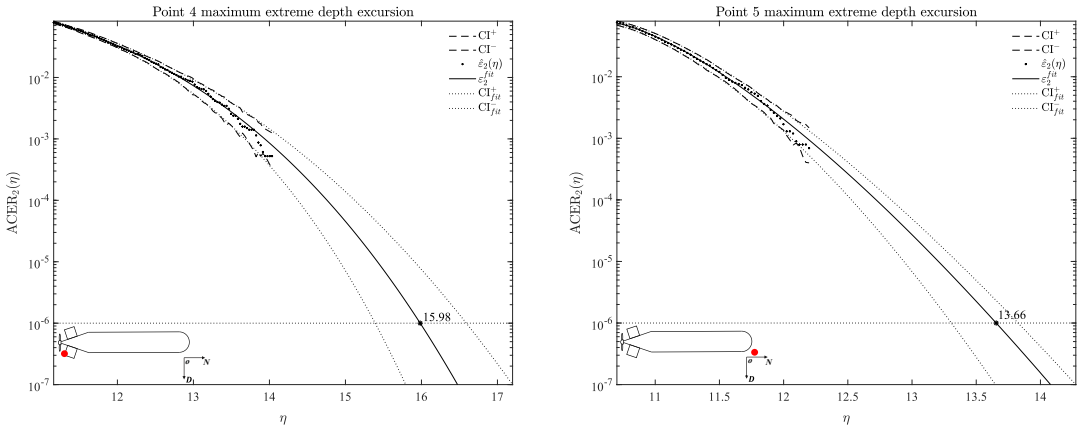

Fig. 14 ACER extrapolation for maximum depth excursion. (a) Point 1. (b) Point 4. (c) Point 5.

Finally, the ACER prediction results are summarised in Table 3. The main findings in this paper are denoted in Fig. 15. The SST's permissible offloading depth region is between 40 m safety depth and 70 m nominal diving depth. However, under a 1.6 m/s extreme current condition, the maximum depth excursion can reach 86 m while the minimum extreme depth is 23.65 m. From the design perspective, it can be noticed that the maximum depth excursion is far from the 190 m collapse diving depth. This indicates that the guidelines are over-conservative in terms of defining the collapse pressure of the SST. With better understanding of the SST, this value can be largely reduced. From the operation perspective, the SST should offload at least 16 m above the upper bound of any subsea installations in order to reduce the risk of collision. Also, the maximum draught of any surface/floating installations should be smaller than 23 m, i.e., the minimum depth excursion when the SST is offloading at the minimum allowable operation depth, in the region of SST operation. Similarly, when an SST is offloading in fields with large draught floating structures, a 16 m minimum safety depth distance should always be maintained.

Table 3 Extreme value responses using ACER method for an exceedance rate of 1×10^{-6}; 95% CI in paratheses.

Extreme depth	**Measurement point**	**Extrapolation value**	**95% CI^{-}**	**95% CI^{+}**
Minimum depth	Point 1	-3.74431	-3.28976	-4.04082
	Point 2	-16.3476	-15.1519	-16.9326
	Point 3	-13.5987	-12.9733	-13.8570
Maximum depth	Point 1	3.75786	3.50877	3.91145
	Point 4	15.9833	15.3909	16.5901
	Point 5	13.6554	13.3068	13.8259

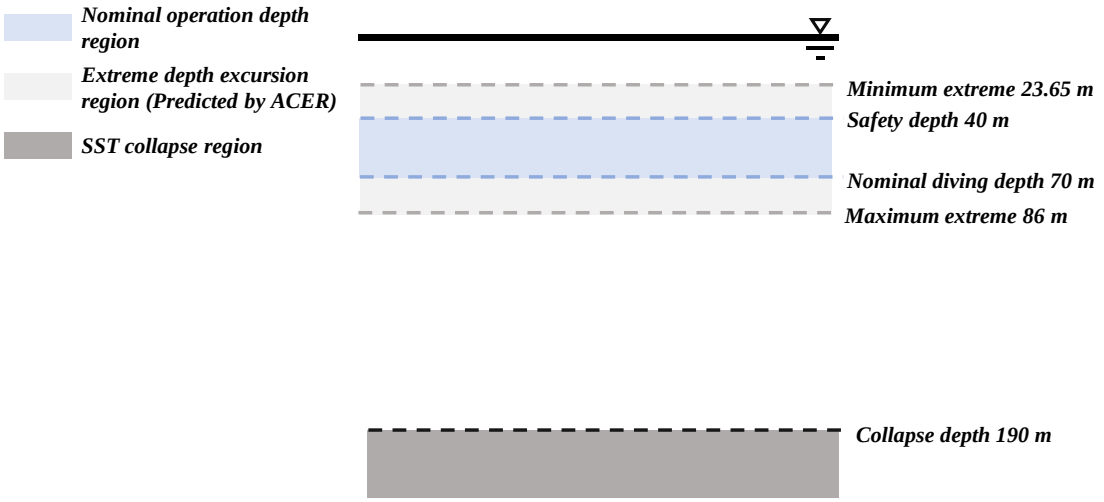

Fig. 15 Depth region of SST offloading.

6. Conclusion

A novel autonomous subsea shuttle tanker concept was proposed as a cost-effective method of transporting liquid CO_2 from shore & offshore facilities to subsea wells for enhanced oil recovery or permanent storage. However, the design of such a large autonomous underwater vehicle has not been detailed investigated. The current existing engineering codes tend to be very conservative by requiring a significant safety factor which will further result in a heavy structural design. Therefore, knowing the maximum response of the SST will benefit the study of such merchant underwater vehicles in two ways: first, knowing the extreme depth excursion unveils the maximum potential off-site of the SST during offloading. This reduces the level of uncertainty and denotes a less conservative design by knocking down the safety factor of the structural design. In addition, the extreme depth excursion can also provide a basis for the decision-makers in terms of SST operation. This study clarifies the maximum and minimum off-site of the SST from its desired offloading reference point. It determines the required minimum safety distance from subsea installations and floating structures during offloading.

This paper studies the extreme response of the SST hovering during offloading. Firstly, a 2D planar model is presented based on the baseline design configurations. The model consists of a rigid SST hull model that considers the hydrodynamic loads acting on the body, the main propeller and two tunnel thrusters located at the front and the aft to keep it stationary under incoming stochastic current. A first-order Gauss-Markov process describes the time-variant stochastic current. The mean current velocity is set to be 1.6 m/s, corresponding to observation data in the North Sea with a return period of 50 years. Later, the SST planar model is streamlined to a linear state-space representation to obtain the controller gain and observer design. During the time-domain simulation, the SST's motion was first measured by the designed Luenberger observer and then passed to the LQR to calculate control inputs. 20 4-hour simulations are performed to get the SST response. Then, the extreme responses with the exceedance rate of 1×10^{-6} from 5 measurement points located at the SST centroid, upper-aft, upper-bow, lower-aft, and lower-bow are studied using the ACER method. The main findings are summarised as follows:

- Effect of k value from 1 to 6 is studied, and the result shows that $k \geq 2$ can provide a very accurate prediction of the SST extreme response during hovering.

- The collapse design of the SST proposed by DNVGL-RU-NAVAL-Pt4Ch1 is very conservative for the SST. The extreme depth excursion happens at the SST aft during hovering, and the maximum depth excursion is 86 m. This means the 19 bar (corresponds to 190 m water depth) collapse pressure can be significantly reduced.
- From an operational perspective, a minimum 16 m safety distance is suggested for the SST hovering. The SST should stay away from any subsea or floating structures with a minimum 16 m distance to avoid a potential collision.
- When the SST is offloading at a 40 m safety depth, the maximum draught of the floating structures in the vicinity should be less than 23 m.

Acknowledgements

The authors declare that they have no acknowledged competing financial interests or personal relationships that could have appeared to influence the work presented in this paper.

References

Bai Y, Bai Q. 2018. Subsea Engineering Handbook MA, USA and Oxford, UK: Gulf Professional Publishing.

Burcher R, Rydill L. 1994. Concepts in Submarine Design Cambridge: Cambridge University Press.

Chai W, Leira BJ, Naess A. 2018. Probabilistic methods for estimation of the extreme value statistics of ship ice loads. *Cold Regions Science and Technology*.146:87-97. DOI: 10.1016/j.coldregions.2017.11.012

DNV. 2010. DNV-RP-C205 Environmental Conditions and Environmental Loads. Oslo, Norway: Det Norske Veritas.

DNV. 2018. Rules for Classification, Naval Vessels, Part 4 Sub-surface Ships, Chapter 1 Submarines. In.

Domps B, Dumas D, Guérin C-A, Marmain J. 2021. High-frequency radar ocean current mapping at rapid scale with autoregressive modeling. *IEEE Journal of Oceanic Engineering*.46:891-899. DOI: 10.1109/JOE.2020.3048507

Ellingsen KE, Ravndal O, Reinås L, Hansen JH, Marra F, Myhre E, Dupuy PM, Sveberg K. 2020. RD 677082-Subsea shuttle system. *Research Disclosure*.

Equinor Energy AS. 2019. RD 662093-Subsea shuttle system. *Research Disclosure*.

Fossen TI. 2021. Handbook of Marine Craft Hydrodynamics and Motion Control. Second ed. West Sussex, UK: John Wiley & Sons.

Gaidai O, Naess A, Karpa O, Cheng Y, Ye R. 2019. Improving extreme wind speed prediction for North Sea offshore oil and gas fields. *Applied Ocean Research*.88:63-70. DOI: 10.1016/j.apor.2019.04.024

Gaidai O, Storhaug G, Naess A. 2016. Extreme large cargo ship panel stresses by bivariate ACER method. *Ocean Engineering*.123:432-439. DOI: 10.1016/j.oceaneng.2016.06.048

Karpa O. 2015. Development of Bivariate Extreme Value Distributions for Applications in Marine Technology [Doctoral theses]. Trondheim, Norway: Norwegian University of Science and Technology.

Luenberger D. 1971. An introduction to observers. *IEEE Transactions on Automatic Control*.16:596-602. DOI: 10.1109/tac.1971.1099826

Ma Y, Xing Y. 2022. Identification of the Safety Operating Envelope of a Novel Subsea Shuttle Tanker. *Ocean Engineering*.Under Review.

Ma Y, Xing Y, Ong MC, Hemmingsen TH. 2021. Baseline design of a subsea shuttle tanker system for liquid carbon dioxide transportation. *Ocean Engineering*.240. DOI: 10.1016/j.oceaneng.2021.109891

Ma Y, Xing Y, Silva MS, Sui D. 2022. Modelling of a subsea shuttle tanker hovering in ocean currents. Proceedings of the 41st International Conference of Ocean, Offshore and Arctic Engineering, 2022 June 5-10, Hamburg, Germany.

Naess A, Gaidai O. 2009. Estimation of extreme values from sampled time series. *Structural Safety*.31:325-334. DOI: 10.1016/j.strusafe.2008.06.021

Naess A, Karpa O. 2015. Statistics of extreme wind speeds and wave heights by the bivariate ACER method. *journal of Offshore Mechanics and Arctic Engineering*.137:021602. DOI: 10.1115/1.4029370

Naess A, Moan T. 2013. Stochastic Dynamics of Marine Structures Cambridge, UK: Cambridge University Press.

Papanikolaou A. 2014. Ship Design: Methodologies of Preliminary Design Dordrecht Heidelberg New York London: Springer.

Pugh DT. 1982. Estimating extreme currents by combining tidal and surge probabilities. *Ocean Engineering*.9:361-372. DOI: 10.1016/0029-8018(82)90029-4

Renilson M. 2018. Submarine Hydrodynamics. 2 editor Cham, Switzerland: Springer International Publishing AG.

481 Sørensen AJ. 2018. Marine Cybernetics (Lecture Notes). Trondheim, Norway: Norwegian University of Science and
482 Technology.
483 Xing Y, Gaidai O, Ma Y, Naess A, Wang F. 2022. A novel design approach for estimation of extreme responses of a subsea
484 shuttle tanker hovering in ocean current considering aft thruster failure. *Applied Ocean Research*.123:103179. DOI:
485 10.1016/j.apor.2022.103179
486 Xing Y, Ong MC, Hemmingsen T, Ellingsen KE, Reinås L. 2021a. Design considerations of a subsea shuttle tanker system for
487 liquid carbon dioxide transportation. *Journal of Offshore Mechanics and Arctic Engineering*.143. DOI: 10.1115/1.4048926
488 Xing Y, Santoso TAD, Ma Y. 2021b. Technical–economic feasibility analysis of subsea shuttle tanker. *Journal of Marine*
489 *Science and Engineering*.10:20. DOI: 10.3390/jmse10010020
490 Xu S, Ji C, Soares CG. 2019. Estimation of short-term extreme responses of a semi-submersible moored by two hybrid mooring
491 systems. *Ocean Engineering*.190:106388. DOI: 10.1016/j.oceaneng.2019.106388
492 Yu S, Wu W, Xie B, Wang S, Naess A. 2020. Extreme value prediction of current profiles in the South China Sea based on EOFs
493 and the ACER method. *Applied Ocean Research*.105:102408. DOI: 10.1016/j.apor.2020.102408
494 Zhao X, Liu Y, Han M, Wu D, Li D. 2016. Improving the performance of an AUV hovering system by introducing low-cost flow
495 rate control into water hydraulic variable ballast system. *Ocean Engineering*.125:155-169. DOI:
496 10.1016/j.oceaneng.2016.08.001
497